Advance Publication by J-STAGE

Electrochemistry

The Electrochemical Society of Japan

Received: January 10, 2024
Accepted: March 6, 2024
Published online: See the URL below.

https://doi.org/10.5796/electrochemistry.24-69009

Review (Invited Paper) *Electrochemistry*, (in press)

The 69th special feature "Frontiers of Molten Salts and Ionic Liquids"

Emerging Molten Salts Based Electrochemical Energy Technologies†

Yu YU,[a,b] Yuhan ZHANG,[a] Han WANG,[a] and George Z. CHEN[a,*]

[a] *Department of Chemical and Environmental Engineering, University of Nottingham, University Park, Nottingham, NG7 2RD, United Kingdom*

[b] *Almath Crucibles Ltd., Unit 2 & 3, The Running Horse, Burrough Green, Newmarket, Suffolk, CB8 9NE, United Kingdom*

* *Corresponding author: george.chen@nottingham.ac.uk*

†Meeting name: 2023 Joint Symposium on Molten Salts (MS 12).

G. Z. Chen orcid.org/0000-0002-5589-5767
Y. Yu orcid.org/0009-0005-9640-8872

Author's Profile

George Z. Chen (Professor of Electrochemical Technologies in the Faculty of Engineering at the University of Nottingham)

He received PhD degree from the University of London and Diploma of Imperial College (DIC) in Physical Chemistry/Electrochemistry in 1992. Following his doctoral studies, he conducted postdoctoral research at the Universities of Oxford, Leeds, and Cambridge from 1992 to 1998. He has garnered recognition through several prestigious awards, such as the TMS Reactive Metals Technology Award (2001, 2004), the Royal Society Brian Mercer Feasibility Award (2007), the E.ON International Research Award (2008), and the Inman Medal (2014). He is now undertaking interdisciplinary research under the theme of "Electrochemical technologies and liquid salts innovations for materials, energy and environment". His current research interests include supercapattery and molten salts based electrochemical processes and devices.

Han Wang (Senior Engineer and Research Fellow at the University of Nottingham)

After obtaining his PhD in molten salt processes for energy applications in the UK, Dr. Wang initiated his career in 2011 at the General Research Institute of Non-ferrous Metals in Beijing, China. Prior to 2022, his work focused on commercializing the production of negative electrode materials for Li-ion batteries using molten salt processes, along with demonstrating green energy applications for commercial use. In 2022, he rejoined George Chen's group to further explore the applications of molten salt-based electrochemical technologies.

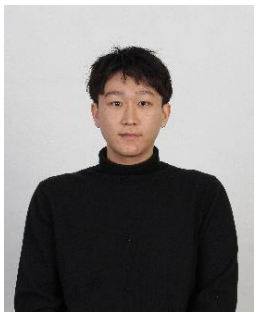

Yuhan Zhang (PhD student in the Faculty of Engineering at the University of Nottingham)

He graduated from University College London, earning an MSc in biochemical engineering in 2018. He moved the University of Nottingham, where he earned an MSc in environmental engineering in 2020. In 2021, he commenced a PhD program under the supervision of Prof. George Z. Chen, with a research focus on the sustainable recovery of metal waste through electrochemical approaches.

Yu Yu (Material Researcher at Almath Crucibles Ltd. and Research Associate at the University of Nottingham)

She graduated from the University of Nottingham in 2022 and received her PhD in Materials Science. Dr. Yu later relocated to Cambridge, where she started the role of a Material Researcher at Almath Crucibles. In the same year, she initiated collaboration with Prof. George Z. Chen, exploring the industrial application of conducting ceramics for recycling metal waste through molten salt electrolysis. Her research interests include developing advanced fabrication techniques for functional ceramic materials and exploring the electrochemical characterization and electrochemical applications of oxide ion conducting/MIEC ceramics.

Emerging Molten Salts Based Electrochemical Energy Technologies

Yu YU,[a,b] Yuhan ZHANG,[a] Han WANG,[a] George Z CHEN[a,*]

[a] Department of Chemical and Environmental Engineering, University of Nottingham: University Park, Nottingham, NG7 2RD, United Kingdom,

[b] Almath Crucibles Ltd.: Unit 2 & 3, The Running Horse, Burrough Green, Newmarket, Suffolk, CB8 9NE, United Kingdom

[*] Corresponding Author. george.chen@nottingham.ac.uk

ORCID:

George Z Chen: 0000-0002-5589-5767

Yu Yu: 0009-0005-9640-8872

Meeting name: 2023 Joint Symposium on Molten Salts (MS 12)

Abstract

Molten salts of inorganic nature are excellent reaction media for various research and industrial uses. Their applications in energy technologies are also wide, including, but not limited to, thermal, nuclear, and electrochemical processes and their combinations. This review aims to capture and analyze selected innovations and developments in recent past, with a specific focus on electrochemical energy storage (EES) technologies. Additionally, it seeks to clarify some fundamental concepts in EES and address prevalent misconceptions, such as those related to Faradaic capacitive/Nernstian processes, battery-like/capacitive cyclic voltammograms (CVs) and galvanostatic charge-discharge curves (GCDs), as well as the calculation of specific energy. The application of molten salts in an emerging EES technology, known as supercapattery, is also explored in this review. This includes the design principle, fundamental calculations, and recent noteworthy demonstrations. Functioning as a hybrid technology, supercapattery combines the merits of both supercapacitor and battery and potentially outperforms each. Drawing insights from advancements in molten salt batteries and molten salt supercapacitors, this review delves into the prospects of developing a sodium-activated carbon (Na-AC) molten salt supercapattery. Through thermodynamic calculations, a specific energy of 445 W h kg^{-1}-AM (where AM denotes the total active mass on both electrodes) is projected, which surpasses the specific energy of 250 W h kg^{-1}-cell achieved by the best commercial lithium-ion battery.

Keywords: molten salt, electrochemical energy storage, supercapattery, thermodynamic calculation

1. Introduction

The immense energy consumption caused by explosive population growth led to severe degradation of the natural environment. With the strong ambitions to achieve emission targets of the Paris Agreement, pressure has been placed on researchers worldwide to develop a low-carbon energy supply chain aiming to limit global warming. Molten salts (MSs) which are inherently ionic in their molten states have been a non-trivial part of the developments of nowadays energy technologies. Owing to their distinctive properties, including low cost, reasonable stability, high heat capacity and excellent heat transfer characteristics, MSs play a prevalent role but are not limited to nuclear and electrochemical processes, thermal and their combinations.

The origins of Molten Salt Reactor (MSR) can be traced back to the late 1940s.[1, 2] The first large-scale MSR experiment, known as the Molten Salt Reactor Experiment (MSRE), commenced in the 1960s and successfully operated for 15,424 hours without encountering any major issues.[3] In comparison with the most commonly used light-water-reactors, a much lower operating pressure (nearly atmospheric) of MSRs led to improved stability and simplified core design which in turn led to increased interest in using MSs as either a fuel salt[4] or a coolant for solid fuel.[5] For instance, the Thorium Molten Salt Reactor-Liquid Fuel 1 (TMSR-LF1) developed by China utilizing lithium-beryllium fluoride as coolant has been licensed for operation recently.[6] Another advantage of MS utilization is the capability of recovering fissile material from used fuel, which has been one major concern controversy surrounding the development of nuclear energy. The spent oxide fuel containing uranium oxide can be reduced in MS (e.g., LiCl) electrochemically, which shares the same principle as the FFC-Cambridge process developed by Chen et al.[7] Due to the wide electrochemical window of MSs, uranium oxide can be directly or electro-lithiothermically reduced at the cathode and reprocessed.[8] This novel recovering route was then confirmed by Stevenson et al.[9] Around 80 % of NiO was directly reduced from the $2NiO\text{-}GeO_2$ binary pellet in molten $CaCl_2$ at 1083 K, followed by dissolution of metallic phase Ni at the anode for separation. Removal of Zr from $ZrO_2\text{-}GeO_2$ precursor was also obtained, which reveals the feasibility of this method.

Since nuclear fuels contain mainly finite elements, alternative renewable energy sources (e.g., solar and wind) are also imperative for accomplishing a sustainable energy supply chain. To overcome the intermittency and unpredictability of renewable energy sources, MS has also been researched in developing appropriate energy storage technologies. One good example is the concentrated solar plant (CSP) utilizing MSs because of their ability to handle high temperatures. During the process, MSs are heated by concentrated solar power and stored in a hot storage tank until it is needed for power generation. Afterwards, the cooled MSs are stored in a cold storage tank for further utilization. An overall efficiency of 98 % could be achieved by the Solar Two power plant operated by the U.S. Department of Energy.[10] As no phase change occurs during the process, this type of thermal storage method is named sensible heat storage (SHS) thus requiring careful consideration of salt type selection. In general, the solar salt ($NaNO_3\text{-}KNO_3$ at 60:40 wt%), the Hitec salt ($NaNO_2\text{-}NaNO_3\text{-}KNO_3$ at 40:7:53 wt%) and Hitec XL® salt ($Ca(NO_3)_2\text{-}KNO_3\text{-}NaNO_3$ at 48:45:7 wt%) developed by DuPont

are typically used in CSP.[11] With the experience in CSP, a nuclear hybrid energy system (NHES) integrating renewable energy sources, nuclear reactors and heat storage systems is designed to fulfil the cascade usage.[12] Similar to CSP, solar heat can be stored by MSs for heating nuclear reactors due to their viscosity and high volumetric heat capacity. Depending on the designs (e.g., two-tank design and the thermocline system), the salts utilized vary (e.g., KCl-$MgCl_2$ and LiF-NaF-KF, respectively) which in turn affects the overall performance.[13-15] Although the utilization of MSs also brings several problems (e.g., corrosion and tritium generation), the unremitting efforts from researchers worldwide on material development, process design and control are imperative to ensure the bright future of those technologies to achieve the sustainable energy transition envisioned.[16]

Despite thermal storage, MSs can also be integrated with renewable energy sources for regenerative fuels processing. This route is quite unique because the electric energy generated by renewable sources can be converted into chemical energy in the fuel itself and ready to be reconverted into electricity for later use. This process uses metal powders, such as iron and aluminium, as energy carriers. These powders have energy densities equal to or exceeding hydrocarbon fuels and have an energy storage capacity (Fig. 1), and they are benign, abundant, and cheap, which are ideal for burning with air to generate heat for a heat engine.[17] Combustion products can be captured with existing cyclonic separation technology and recycled back to metal using clean energy (e.g. FFC-Cambridge process), resulting in a completely closed-loop energy-carrier cycle.

Besides, carbon dioxide can also be collected and reduced into regenerative fuels via MS electrolysis, as shown in Fig. 2. The idea was initially proposed by Chen's research group in 2006, using molten salt heated by solar energy for the reduction of CO_2 into solid carbon.[18] Afterwards, Licht et al. confirmed the feasibility of this method using molten Li_2CO_3 with 34-50 % solar efficiency.[19] In general, the overall process efficiency and product formation can be affected by but not limited to salt type (e.g., molten carbonates), operating temperature, CO_2 partial pressure and anode selection.[20, 21] Furthermore, well-established regenerative fuels (e.g., H_2 and CH_4) can also be produced via CO_2/H_2O co-electrolysis in molten carbonates and hydroxides eutectic.[22]

MSs are also widely used as electrolytes in electrochemical energy storage (EES) devices, involving batteries, supercapacitors, and redox flow battery & rechargeable fuel cells.[23] EES technologies are crucial for present and future energy infrastructure for enabling efficient energy storage, promote renewable energy utilization, power portable electronics and electric vehicles, and offsetting the drawbacks of power production using stochastic renewable sources. Typical EES devices, rechargeable batteries with high energy capacity and supercapacitors with high power capability, are usually manufactured in modules or units to meet the energy demand flexibly. Material selection is imperative to design a functional and efficient EES device, especially in MS based EES devices due to the high operating temperature. Owing to the superb characteristics of MSs, the utilization of them as electrolytes in EES devices has gained much attention. For example, the Na-$NiCl_2$ Zero Emissions Batteries Research Activity (ZEBRA) batteries have been considered the most attractive MS batteries and manufactured commercially by the FZSoNick Group.[24] A solid β-Al_2O_3 membrane and the molten sodium tetrachloroaluminate ($NaAlCl_4$) are used as the electrolyte, which offer the conduction of Na^+ and the reversible conversion between molten $NiCl_2$ and solid-state Ni on the positrode during discharging and charging. The reported energy efficiency was close to 100 % with specific energy varying from 90-120 W h kg^{-1}.[25, 26] Besides, abundant elements, such as magnesium, calcium and aluminium, are also utilized in MS batteries with reasonable life cycle and efficiency.[27-29] The excellent ability of MSs to accommodate these earth-abundant metal negative electrodes offers strong economic advantages on the utilization of MSs-based batteries. Furthermore, MSs are also dominant electrolytes for liquid metal batteries (LMBs) and molten-air batteries (MABs).[30, 31] Recently, a Na-O_2 was developed by Zhu et al. in $NaNO_3$-KNO_3-$CsNO_3$ at 443 K with excellent energy and power densitie.[32] Moreover, the utilization of liquid Na negative electrode avoids the dendrites from solid Na deposition in typical batteries. The mentioned research indicates the feasibility of MSs batteries in terms of promising efficiency and stability. Further development on materials and designs is still required for broader utilization of MS batteries in future.

Unlike rechargeable batteries, supercapacitors have different advantages, such as high-power capability (e.g., 10 kW kg^{-1}) and long cycle life. Since electrical charges are stored in capacitive processes, the charging and discharging are much more rapid than rechargeable batteries which leads to a higher power density of supercapacitors. Details on the related principles are given in the following section. In comparison with typical

aqueous or organic electrolytes, the utilization of inexpensive MSs in supercapacitors offers a wider electrochemical stability window and high ionic conductivity. In 2013, $LiNO_3$-$NaNO_3$-$CsNO_3$ eutectic mixture was used in a symmetrical supercapacitor. The specific cell capacitance obtained was 31.5 F g^{-1} with a specific energy of 22.8 W h kg^{-1}.[33] Further research was carried out by Wang et al. in molten $AlCl_3$-NaCl-LiCl employing activated carbon electrodes.[34] Improved specific energy (50.4 W h kg^{-1}) was obtained at 397 K with promising cycling stability (99.8 % capacitance retention after 10000 cycles) demonstrating the feasibility and the promising potentials of MS supercapacitors.

To meet future energy requirements and fulfil various commercial requirements, continuous research is ongoing aimed to increase energy density, faster charging, longer cycle life, and improved sustainability. A novel supercapacitor-battery hybrid EES device, supercapattery, is promising to be the 3rd generation EES device.[35, 36] As the Ragone Plot illustrated in Fig. 3, by combining the merits of rechargeable batteries and supercapacitors, supercapatteries are potentially to achieve comparable performance to supercapacitor in power capability and cycle life, and to battery in energy capacity. This hybrid technology can be achieved by synthesizing hybrid electrode materials from supercapacitors and batteries or combining a supercapacitor and battery electrode in a EES device.[37-40] Although there is a paucity of research on MSs-based supercapattery, knowledge and experiences could be borrowed from the research on MS batteries and MS supercapacitors to motivate its development. Here, this review will focus on (1) clarifying the hybrid battery-capacitor mechanism for this new EES technology, (2) discussing the prospects of MS supercapattery, and (3) proposing a hypothetical MS Na-AC supercapattery and analysing the feasibility in aspect of thermodynamics.

2. Hybrid battery-capacitor mechanism of a supercapattery

As mentioned earlier, both batteries and supercapacitors serve as EES devices, with the supercapattery emerging as a hybrid technology combining features of both. In Fig. 4 (a), a conceptual representation of a general EES device is presented, capturing the essence of a supercapacitor, rechargeable battery, and a supercapattery (or supercabattery). Figure 4 also provides a visual depiction of the representative electrochemical features, including cyclic voltammogram (CV) and galvanostatic charging-discharging plot

(GCD), for each device type. It is essential to clarify the fundamentals of EES devices, batteries, and capacitors before delving into supercapatteries.

2.1. Electrode processes in EES devices

In all EES devices, the electrode processes play a pivotal role in charge storage. Figure 4 (a) depicts a cross-section of a representative single EES cell, comprising a positive electrode, a negative electrode, and an electrolyte separator. The terms 'negatrode' and 'positrode' correspond to the negative and positive electrodes, respectively. Electrodes are designated based on their electrical polarities, wherein the positive electrode always maintains a higher (or more positive) potential than the negative electrode. Current flows from the positive to the negative electrode through the external circuit, while electrons move in the opposite direction.

In many publications related to EES, the positive electrode is often referred to as the cathode, where the reduction reaction occurs, while the negative electrode is termed the anode, where the oxidation reaction occurs. In the context of rechargeable EES devices, during discharge, reduction occurs at the cathode, and oxidation occurs at the anode. However, during charging, the oxidation occurs at the so-called cathode, while the reduction reaction happens at the so-called anode. Such use of cathode and anode terminology in EES devices can deviate from both electrical and electrochemical principles, as well as the manufacturer's instructions, potentially causing confusion or misunderstanding. The terms 'negatrode' and 'positrode' offer an alternative, helping to avoid this confusion.

Electrode processes occur on both the negatrode and positrode, involving one or a combination of electric double-layer (EDL) capacitive, Faradaic capacitive (pseudocapacitive), and Nernstian (battery-like) mechanism.[36] The EDL discharging and charging are physical processes at the electrode/electrolyte interface, encompassing electrostatic attraction/repulsion and specific dis-/absorption. This results in the EDL capacitance. Ideally, no electron transfer takes place across the electrode/electrolyte interface, and the storage of electric charge and energy involves no chemical changes within the solid phase of the electrode. The EDL exhibits capacitor-like behaviour.

In contrast to the EDL process, Faradaic processes encompass electron transfer reactions occurring at the interface between an electrode and its solid or liquid electrolyte phase, capable of accepting or donating electrons. Faradaic processes involve two mechanisms: Faradaic capacitive and Nernstian processes. Nernstian storage arises from reversible electrode reactions primarily governed by the Nernst equation, constituting a battery-like and non-capacitive process. The Faradaic capacitive process is associated with a rapid electron transfer, resulting in pseudo-capacitance.

The capacitive nature of both pseudocapacitive and EDL storage processes, along with the fact that both pseudocapacitive and Nernstian storage fall under Faradaic processes, has led to ongoing confusion, particularly with the introduction of pseudo-capacitance. To address this, efforts have been made to qualitatively apply the band model for semiconductors, aiming to provide insight into the origin of pseudo-capacitance. Further discussion on distinguishing between capacitive and non-capacitive Faradaic processes will be presented in the following two sections.

2.2. Rechargeable battery basics

An electrochemical rechargeable battery operates by converting chemical energy into electrical energy through reversible Nernstian reactions, constituting a non-capacitive Faradaic process, as illustrated in Equation (1) below:

$$O + ne^- \rightleftharpoons R \qquad \text{Equation (1)}$$

The battery typically comprises two electrodes separated by an electrolyte separator. During the charging phase, the battery undergoes redox reactions, where the positrode experiences oxidation, and the negatrode undergoes reduction. Ions or molecules are released from one electrode and either intercalated or deposited onto the other electrode, thereby storing energy. In the discharge phase, the stored energy is released through reverse redox reactions, with the positrode now undergoing reduction and the negatrode oxidation. As ions or molecules migrate back to their original positions, an electric current is generated.

The Nernstian process can arise from localised reversible electron transfer reactions occurring in a redox-active coating on an electrode. In such instances, the CV typically exhibits a bell-shaped curve, complemented

by its mirror reflection, as illustrated in Fig. 5.[43, 44] The potential of the current peaks on the CV is determined by the redox potential of the material. The current response to the potential changes can be expressed by Equation (2), derived from the Nernst and Randles-Sevcik equations:[45]

$$i = \frac{n^2F^2A\Gamma_t \exp\left[(E-E^0)\frac{nF}{RT}\right]}{RT\left\{1+\exp\left[(E-E^0)\frac{nF}{RT}\right]\right\}} \quad \text{Equation (2)}$$

where n is the number of electrons transferred between the reduced and oxidised sites, F is the Faraday constant, A is the electrode area, $\Gamma_t = \Gamma_o + \Gamma_r$ represents the total surface covered by the reduced and oxidised sites, R is the ideal gas constant, and T is the absolute temperature.

The GCDs in Fig. 5 (b) follow the equation below, representing a unique form of the Nernst equation:[45]

$$E = E^o + \frac{RT}{nF}\ln\left(\frac{1-x}{x}\right) \quad \text{Equation (3)}$$

Here, $x = \Gamma_r / \Gamma_t$ denotes the mole fraction of reduced species (or sites) on the electrode surface at time t. Under reversible conditions, where the process is governed by the Nernst equation, x is related to the amount of charge passed by Faraday's law:

$$x = \frac{it}{nF\Gamma_t} \quad \text{Equation (4)}$$

where i is constant, and the energy calculation from a GCD recorded in a two-electrode cell involves integrating the plot:

$$W = \int_0^t iU\mathrm{d}t = i\int_0^t U\mathrm{d}t \quad \text{Equation (5)}$$

where W is the energy and U is the potential recorded at t. Due to the strong potential dependence of the electrode reaction, the GCD in Fig. 5 (b) exhibit potential plateaus within a narrow potential range. When the Nernst reaction occuring in the electrode materials is reversible, the shapes of the CVs and GCDs are symmetrical in horizontal and vertical orientations, respectively.[42]

Less reversible behaviour is frequently observed in the testing of battery electrode materials. In these cases, the peak potential of oxidation on the CVs tends to shift positively, while that of reduction shifts negatively. On the GCDs, charging induces a deviation with the potential rising upward over time from the plateau, and

during discharging, the potential decreases downward. Figure 4 (b1)-(b3) illustrates the anticipated deviations in CVs and GCDs for a battery and its electrodes. This behaviour largely contributes to the relatively low energy efficiency of a battery.

2.3. Supercapacitor basics

The fundamentals of supercapacitors closely resemble those of conventional capacitors widely used today. In conventional capacitors, two types exist, each comprising a positive electrode plate, a negative electrode plate, and an insulating medium—either dielectric or ionic electrolyte—situated between the two plates. The electrolyte capacitors, owing to the presence of freely mobile ions in the electrolyte bulk, typically exhibit capacitance in the mF range. This is several orders of magnitude higher than that observed in dielectric capacitors, which generally operate in the μF range.

In both dielectric and electrolyte capacitors, the stored charge is directly proportional to the strength of the applied electric field or voltage (U) between the positive and negative plates. This proportionality is expressed as capacitance (C), linking Q and U through Equation (6) below:

$$C = \frac{Q}{U} = \frac{\varepsilon_0 \varepsilon A}{d} \qquad \text{Equation (6)}$$

Here, C depends on the dielectric constant (or relative permittivity, ε) of the dielectric medium and is proportional to the ratio of the area of the electrode/dielectric interface (A) to the separation distance between the two electrode plates (d). $\varepsilon_o = 8.854 \times 10^{12}$ F m^{-1} represents the vacuum permittivity.

Equation (6) can be mathematically transformed into various forms to suit different experimental tests. One relevant test involves the current response to voltage variation, as derived by rearranging Equation (1) to $Q = CU$. By differentiating this equation with respect to time (t) and considering C as a constant, the following equation is obtained:

$$\frac{\mathrm{d}Q}{\mathrm{d}t} = C\frac{\mathrm{d}U}{\mathrm{d}t} + U\frac{\mathrm{d}C}{\mathrm{d}t} = C\frac{\mathrm{d}U}{\mathrm{d}t} \qquad \text{Equation (7)}$$

If the applied voltage varies linearly with time (i.e., $U = U_o + vt$, where t is the time, U_o is the starting voltage, which may be zero, and v is the voltage scan rate), then $dU/dt = v$. Considering that $dQ/dt = i$ (current), Equation (7) can be further simplified to correlate the current with the scan rate:

$$i = Cv \qquad \text{Equation (8)}$$

Equation (8) shows that the current (i) flowing through a capacitor is proportional to the linear rate of change of voltage (v), independent of the voltage itself (U). It is important to note that v is positive for an increasing voltage and negative for a decreasing voltage. Consequently, the current can be either positive or negative, depending on the direction of the voltage scan. Specifically, if the voltage scan direction is abruptly reversed while maintaining the same rate, the current will jump from a positive value to a negative value. This characteristic of Equation (8) manifests in the rectangular shape of the *i*-*U* plots at various voltage scan rates, as illustrated in Fig. 6 (a). The rectangular shape of *i*-*U* plots (CVs) serves as an experimental criterion for qualitatively assessing the capacitive behaviour of a device or electrode constructed from synthetic pure or composite materials of interest.

When a constant current is applied for either charging (positive current) or discharging (negative current) the capacitor, Equation (8) anticipates a steady rate of voltage increase during charging or decrease during discharging. Consequently, if the voltage of the capacitor is plotted against time during a cycle of constant current charging and discharging, which essentially involves integrating Equation (8), a triangular curve is expected in the GCD plot, as shown in Fig. 6 (b).

A capacitor possesses the ability to store electric energy. When a voltage (U) is applied to the capacitor for a short time, a small amount of work (dW) is accomplished to move a quantity of charge (dQ), which accumulates at the electrode/dielectric medium interface. This work is expressed as the product of voltage and charge, i.e., $dW = UdQ$. Assuming negligible heat loss, dW equates to the energy stored in the capacitor and can be linked to Equation (6), yielding the following equations after integration:

$$dW = UdQ = \frac{Q}{C}dQ \qquad \text{Equation (9)}$$

$$W = \int_0^Q \frac{Q}{C}dQ = \frac{1}{2}\frac{Q^2}{C} = \frac{CU^2}{2} \qquad \text{Equation (10)}$$

It is noteworthy that Equation (6) indicates that the voltage of a capacitor is proportionate to the accumulated charge. Additionally, a practical capacitor always has a maximum tolerable voltage, U_{max}, defined by Equation (10).

The power output (P) from a capacitor can be derived by dividing W by t, the time required for a complete discharge of the capacitor, i.e.,

$$P = \frac{W}{t} = \frac{CU^2}{2t} \qquad \text{Equation (11)}$$

Evidently, the maximum power output is determined by the shortest discharging time, which cannot be directly derived from the aforementioned equations.

It is a recognised fact that any electric power source has an internal resistance referred to as the equivalent series resistance, or simply ESR. When the power source is connected to a load, R_L, within the circuit, and given the voltage of the power source as U, the current passing through the circuit is $i = U/R$, where $R = R_L$+ESR. The power transferred from the source to the load is $P = iU = i^2R$, leading to the derivation of Equation (12):

$$P = \left(\frac{U}{R_L+\mathrm{ESR}}\right)^2 R_L = \frac{R_L U^2}{(R_L+\mathrm{ESR})^2} \qquad \text{Equation (12)}$$

It is worth to note that the fundamental principles outlined above for conventional capacitors are equally applicable supercapacitors.

1st-generation supercapacitors

First-generation supercapacitors operate based on the interfacial charge storage mechanism, where electric double layer facilitate charge storage through electrostatic adsorption of ions at the electrode and electrolyte interface. This process occurs simultaneously on both positive and negative electrodes without involving chemical reactions.

The storage mechanism shares similarities with conventional electrolyte capacitors, but the specific capacitance (C_s, F g^{-1}) achieves a significant increase by orders of magnitude. This enhancement is achieved through the exploitation of the vast specific surface area (measured in m^2 g^{-1}) of porous inert materials, such

as activated carbon (AC).[46] These first-generation supercapacitors are commonly known as electric-double layer capacitors (EDLCs).

Despite being widely considered as physical energy storage, ions are solvated in the bulk electrolyte solution, with reduced solvation when adsorbed at the 'electrode | electrolyte' interface (or in the EDL) which is the case for a porous carbon negative electrode in contact with an aqueous electrolyte. Many schematic depictions of the EDL on a planar electrode surface can be found in the literature, with examples provided in works like Bard and Faulkner.[45] Figure 7 (a) specifically represents the EDL on a porous carbon negative electrode. It is crucial to note that charge storage in EDLC still involves changes in chemical bonding, hence it is not purely physical, nor solely chemical.[36]

Limitations can arise from the interplay of specific surface area, porosity, strength, and electronic conductivity in supercapacitor materials. Essentially, higher porosity in carbon translates to a larger specific surface area, but this comes at the cost of reduced strength and conductivity. Compounding this challenge is the fact that not all internal surface areas, including those within the walls of micro-pores, are accessible for ions in activated carbon during charge storage. For activated carbons, despite boasting specific surface areas typically in the range of 1000-2000 $m^2\ g^{-1}$, the specific capacitance often remains below 100 F g^{-1}.[47] To address these issues, nanomaterials like carbon nanotubes (CNTs) and graphene have been explored as electrodes in EDLCs, aiming to improve the overall performance. However, the specific capacitance of first-generation supercapacitors struggles to surpass 200 F g^{-1}.[48-50]

2nd-generation supercapacitors

2nd-generation supercapacitors operate on a pseudocapacitive storage mechanism. In this mechanism, charge storage within the electrode involves rapid and reversible electron transfer or Faradaic reactions across a wide potential range. The concept of pseudo-capacitance links Faradaic reactions and supercapacitors, initially associated with the behaviour of adsorbed or deposited monolayer species on electrode in the early 1960s.[51, 52] Ruthenium dioxide (RuO_2) was possibly the first reported redox-active material, capable of exhibiting rectangular CVs similar to a capacitor.[53] Similar observations of rectangular CVs have been reported for both electronically conducting polymers (ECPs)[54-56] and other transition metal oxides (TMOs).[57-60]

In contrast to porous activated carbons, where charge is stored in the EDL in a two-dimensional manner, redox-active materials achieve capacitance through charge storage within the three-dimensional structure of the material, as illustrated in Fig. 7 (b). Consequently, the specific capacitance of redox-active materials is approximately an order of magnitude larger than that of EDL materials.

It is worth to emphasise that pseudo-capacitance, while Faradaic in nature, is distinct from the Nernstian process, as clarified in Section 2.1. It should not be associated with current peaks on CVs. In terms of performance, pseudo-capacitance exhibits similarities to double layer capacitance, manifesting as rectangular CVs and triangular GCDs, as demonstrated in Figs. 4 and 6. Figure 7 further provides two examples of measured CVs linked to EDL capacitance and pseudo-capacitance, facilitating additional comparison and clarification.

Confusions regarding the differentiation between capacitive Faradaic storage and Nernstian storage has emerged with the introduction of pseudo-capacitance in TMOs and ECPs. Recently, a qualitative explanation was proposed[44, 62] based on band theory for semiconductors.[45, 63] This explanation is briefly described with reference to Fig. 8.[61]

The evolution of energy levels is illustrated, ranging from those of individual and separated metal atoms to clusters containing 2, 5, 20 and 10^{20} atoms. Progressing from left to right, the original orbits of the atoms are split into more sub-orbits with different energy levels, and the gap between neighbouring energy levels of sub-orbits becomes smaller. As depicted in Fig. 8 (c), the valence electron occupation state varies in different band structures, resulting in distinct conductivity behaviour, namely insulator, semiconductor, and metal.

According to the band model, Nernstian behaviour corresponds to electron transfer to or from isolated redox centres, such as those in a solid insulator or liquid electrolyte, where the valence electrons are localised. In simpler terns, all the transferred electrons enter or leave the orbits with the same energy level (of different redox centres), as illustrated on the far-left side of Fig. 8. Consequently, the Faradaic reaction occurs at potentials within a narrow range around the equilibrium potential, E^{o}, leading to current peaks on CV or potential plateaus on GCD, as discussed in Section 2.2.

In the semiconductor region, there are numerous orbits with very closely spaced energy levels across a wide band. Consequently, electron transfer can occur over a broad range of potentials, with each small change in potential facilitating electron transfer. This results in a constant current flow in a capacitive manner, characterized by a linearly varying potential or a linearly varying potential under a constant current. As discussed in Section 2.3., this phenomenon leads to the generation rectangular CVs and linear GCDs. This behaviour is observed in semiconducting TMOs and is comparable to the delocalisation of electrons in conjugated chemical bonds, as seen in ECPs. This capacitive Faradaic process forms the basis of pseudo-capacitance in the context of supercapacitors, a concept that was only recently recognized.[42, 44, 64]

While materials with pseudo-capacitance exhibit a larger specific capacitance, they face challenges due to their semiconducting nature. In practical supercapacitors, maximizing the energy capacity involves loading as much active material as possible, typically achieved by increasing the coating thickness of the active material. Unfortunately, this approach has limited effectiveness due to high electrode resistance. The elevated resistance not only diminishes the power capability in accordance with Equation (12) but also hinders electronic access to all active sites within the thick coating.

Pseudocapacitive materials face an additional challenge related to the access of charge-balancing ions to the active sites within the semiconducting material, particularly when in the form of a thick coating, due to slow solid-state diffusion. This results in a significant compromise in specific capacitance and power capability. Moreover, the repeated ingress and depletion of ions in the electrode material inevitably lead to cyclic stress changes at microscopic levels, causing structural alterations or even disintegration around the active sites. As a consequence, the cyclic charging-discharging life of a pseudo-capacitor (~10^3 cycles) is much shorter than that of an EDLC (> 10^5 cycles).

2.4. Supercapattery: merging capacitive and Nernstian storage mechanism

Aiming to combine the merits of a supercapacitor and a rechargeable battery, supercapattery employs both capacitive and Faradaic mechanisms.[65, 66] This hybrid system offers numerous combination options, as capacitive storage can be either EDL or pseudocapacitive. Supercapattery can be achieved by hybridising materials or electrodes within the same device. For example, the battery or Nernstian electrode can serve as

either the positrode or negatrode, with the EDL or Faradaic (pseudo-) capacitive electrode being the opposite one.

Supercapattery behaviour can arise from various materials, such as heat-treated nickel hydroxide films in aqueous KOH.[67] Composites of manganese oxides (MnO_x, $1.5 < x \leq 2$) with carbon nanotubes or graphene can also store charges through mixed mechanisms.[68-70] Additionally, engaging electron transfer reactions of soluble species, such as iodide ions, with EDL capacitance of a porous carbon electrode is another effective way to combine capacitive and Nernstian mechanisms.[35, 71-73]

In fact, the combination of capacitive and lithium storage electrodes has been reported in earlier literatures.[74] The term 'lithium-ion capacitor' first appeared also in 2007.[74-76] Various terms, such as 'redox capacitors', 'Li-ion capacitors', and 'pseudo-capacitors' are also used in the literature to describe hybrid EES devices.[61, 77-82] These hybrids store charge differently from a capacitor. However, the use of the term 'capacitor' in their names has led to the misuse of capacitance as a performance indicator.[83] When considering a battery-supercapacitor hybrid device as a capacitor, incorrect calculation of the stored energy can occur. A previous review extensively illustrates this issue, particularly concerning the use of redox electrolytes in supercapacitors.[35]

For unambiguous classification and comparison, the generic name supercapattery (= supercapacitor + battery) was proposed in 2007, with laboratory demonstration following later.[39, 84] The term supercapattery was relatively rare in the literature before 2015, however, interest in it has been rapidly growing. This increased interest is partly driven by curiosity and exploration of new and improved EES mechanisms, materials, and devices beyond supercapacitors and rechargeable batteries.[65, 85, 86] Another, more fundamental reason is related to pseudo-capacitance, which unfortunately has been misused to account for the behaviour of many new transition metal compounds capable of Nernstian storage.

To accurately characterize non-capacitive behaviour in supercapatteries, it is essential to employ appropriate experimental and theoretical tools. This approach allows for a thorough elucidation of the relationships between physicochemical observations and electrical responses, avoiding the misuse of capacitance or pseudo-capacitance to describe such behaviour.

It is essential to comprehend supercapattery from an electrochemical perspective. Figure 9 depicts the calculated GCDs of three types of EES devices: (a) featuring a typical battery negatrode and a pseudocapacitive positrode, (b) incorporating a lithium battery negatrode and a pseudocapacitive positrode, and (c) designed with a ELD capacitive positrode and a lithium-carbon battery negatrode. The fundamental calculations are briefly introduced below, based on the relations between the two electrodes, with more detailed calculation available in Ref[36].

Firstly, the charges passing through the Nernstian (Q_{bat}) and capacitive (Q_{cap}) electrodes must be equal, as expressed by:

$$Q_{bat} = m_{bat}Q_{sp} = m_{cap}C_{sp}\Delta E_{cap} = Q_{cap} \quad \text{Equation (13)}$$

$$\Delta E_{cap} = \frac{m_{bat}Q_{sp}}{m_{cap}C_{sp}} \quad \text{Equation (14)}$$

where m_{bat} is the weight of Nernstian electrode, m_{cap} is the weight of capacitive electrode, Q_{sp} is the specific charge, and C_{sp} is the specific capacitance.

Equation (14) is valuable for designing supercapattery, disregarding whether the capacitive or Nernstian electrode serves as the positrode or negatrode. Increasing m_{bat}/m_{cap} maximises ΔE_{cap}.

Secondly, equal currents occur on both electrodes at any time. Equation (15) governs the relation, linking with Nernst Equation (3) and (4) (charging on the positrode or discharging on the negatrode).

$$i_{cap} = m_{cap}C_{sp}\frac{dE_{cap}}{dt} = \frac{nF\Gamma_r}{t} = i_{bat} \quad \text{Equation (15)}$$

Equation (3) and (15) were used to calculate the GCDs in Fig. 9 (a)-(c). The combination of battery and supercapacitor electrode materials within a single EES device can yield behaviour that appears either similar to a capacitor, demonstrating linear voltage variation with time as illustrated in Fig. 9 (b) and (c), or closely resembling that of a battery, showing non-linear voltage-time relations in Fig. 9 (a). In both scenarios, the shaded area under the discharging branch of the GCD is proportionate to the discharged energy.

When the GCD of a cell exhibit non-linear behaviour, it more closely resembles batteries than supercapacitors. In such cases, calculating the energy value involves integrating the non-linear plot, and the energy capacity of

the cell should be determined by integrating the GCD of the cell using Equation (5), rather than relying on Equation (10). Moreover, it may be beneficial to refer to these devices as supercabatteries to distinguish them from supercapatteries that exhibit behaviour more like supercapacitors.

Equation (10) is applicable to the scenarios of linear GCDs depicted in Fig. 9 (b) and (c). These hybrid devices deviate from both conventional supercapacitors and batteries in terms of charge storage mechanisms but demonstrate enhanced technical performance. The array of such hybrid devices is experiencing exponential growth, warranting the introduction of new terms, thus prompting the proposals of supercapattery and supercabattery.

In practical situations, charging capacitive electrodes, whether EDL or Faradaic, is highly reversible and therefore rapid. Consequently, in the calculations, the charging rates of the cell are assumed to be such that the Nernstian electrode can respond in accordance with Equation (3) and (4). These conditions are indeed achievable, as demonstrated by the experimentally recorded GCDs in Fig. 9 (d)-(f).[38, 40, 88]

Table 1 presents the calculation results corresponding to Fig. 9 (a)-(c), suggesting that a combination of an activated carbon electrode and a metal electrode is more favourable for achieving optimal performance. In a practical application, Lin et al. developed a densified, nitrogen (N)-doped, and nanoperforated graphene (DNPG) capacitive electrode.[89] They assembled a Li/DNPG cell to evaluate the energy density of the hybrid power device using a 1 mol L^{-1} $LiPF_6$ electrolyte. Remarkably, this Li/DNPG hybrid EES device exhibits behaviour similar to that of a supercapattery.

Typically, carbon exhibits low packing density, resulting in a capacitor with low volumetric capacitance when used as electrodes. Additionally, the use of low-density carbon electrodes can lead to the absorption of excessive electrolyte, significantly increasing the device weight without a corresponding increase in capacitance. Although graphene is denser, it can hinder ion diffusion. To address these challenges, molten sodium amide was employed to condense the expanded graphene (EG). Acting as a mild etching reagent, it created 3-5 nm in-plane pores on the oxygen-containing plane of graphene, as illustrated in Fig. 10 (a). This modification helps facilitate ion transport / diffusion in dense graphene stacks as illustrated in Fig. 10 (b) and

(c). Furthermore, sodium amide induced nitrogen doping, known as an effective method, to enhance the pseudo-capacitance of carbon.[90, 91]

With these advantageous features, the densified nitrogen doped nano-porous graphene (DNPG) delivers the highest volumetric capacitance (522 F cm^{-3}) achieved in a KOH solution to date. Moreover, in a lithium-ion battery electrolyte, since the device was dis-/charged between 1.5 and 4.5 V, the capacity 206 mA h g^{-1} of DNPG at 0.5 A g^{-1} corresponds to a specific energy of 618 W h kg^{-1} at a specific power of 1500 W kg^{-1}, and an energy density of 740 W h L^{-1}at a power density of 1800 W L^{-1}, making it competitive with $LiFePO_4$.[92-95]

3. Energy storage in molten salt electrochemical devices (battery and supercapacitor)

To date, extensive research efforts have been dedicated to exploring supercapattery configurations using ILs as electrolytes.[96] ILs play a pivotal role as electrolyte materials in EES devices due to their distinct advantages over aqueous and organic electrolytes. Compared to aqueous electrolytes, ILs offer a broad voltage window, enabling higher energy density and enhancing the overall performance of EES devices. Additionally, ILs exhibit commendable thermal stability and are non-flammable, reducing the likelihood of decomposition and associated safety risks in comparison to organic electrolytes. When combined with appropriate additives, IL electrolytes can mitigate dendrite growth on metal anodes and the formation of an unstable solid electrolyte interphase (SEI) in typical batteries. However, it is essential to note that the high viscosity of ILs can lower ionic conductivity, and their high costs are also unfavourable.

The high temperature counterpart of ILs is MSs, and both ILs and MSs are liquid salts in nature. MSs offer some unique advantages over ILs. They are low cost, wide electrochemical windows. At temperatures slightly higher than its melting point (e.g., by 50 ^{o}C), an inorganic MS becomes water-like in viscosity and hence offers high ionic conductivity, which is beneficial to achieve high-performance EES devices.[32, 34, 97, 98]

One example is the high temperature MS ion-air battery developed by Zhang et al. in 2021, which achieved a high specific energy density of 380.3 W h kg^{-1} and a good cycling performance at 800 °C for 70 cycles. Figure 11 (a) shows the battery structure, where the negatrode is Fe/FeO_x, and a quasi-solid-state (QSS) electrolyte was used which consists of the molten $NaCO_3$-K_2CO_3 eutectic (NaK) and yttrium stabilised zirconia (YSZ)

nanoparticles. The QSS electrolyte has a good conductivity at working temperature, 800 °C, approximately ~0.22 S cm^{-1}, only slightly lower than that of molten NaK electrolyte (~0.42 S cm^{-1}). The electrode reactions are as follows.

Positrode $3/4O_2 + 3e^- \leftrightarrow 3/2O^{2-}$ Equation (16)

Negatrode $Fe + 2O^{2-} \leftrightarrow FeO_2^- + 3e^-$ Equation (17)

Figure 11 (b) illustrates that the cell voltage profile gradually decreased as the discharging current density increased from 0.5 to 2 mA cm^{-2}, while the specific capacity remained at ~1300 mA h g^{-1} based on the mass of iron on the negative electrode, closely approaching the theoretical specific capacity of 1430 mA h g^{-1}. All the charge/discharge curves from the 10th to the 70th cycles are nearly identical, with an approximately constant discharge specific capacity of around 1300 mA h g^{-1}, indicating the high stability of the QSS molten salt ion-air battery. Moreover, no dendrites were observed during repeated discharging and charging cycles.

MS electrolytes are not exclusively limited to high operating temperatures like 800 °C. Some salt mixtures exhibit eutectic melting behaviour at lower temperatures, allowing for a reduced working temperature. Wang et al.[98] presented a Li||Sb-Pb liquid metal battery employing a molten mixture of LiF-LiCl-LiI (20:50:30 mol%, T_m = 430 °C) as the electrolyte. Note that at the working temperatures (450 to 600 ºC), both Li metal and Sb-Pb alloy are liquid, and such cells are known as all liquid metal battery. Fig. 12 illustrates the structure of such an all liquid metal cell upon charge and discharge, and the characteristic GCD profiles. At the operational temperature of 450-500 °C, both the metal negatrode (Li, T_m = 180.5 °C) and positrode (Sb-Pb 30:70 mol% for the cell, and the eutectic composition, Sb-Pb 18:82 mol%, T_m = 253 °C) exist in the liquid state. This battery successfully operated at current densities up to 1000 mA cm^{-2} during discharge and charge cycles. Even at the highest current density, the cell performed at 54 % of its theoretical capacity, without incurring permanent damage, underscoring the importance of long-term electrode stability. This remarkable performance is attributed to the high conductivity of the MS electrolyte, ultrafast charge-transfer kinetics at the electrode-electrolyte interface between the liquid metal and molten salt, and rapid mass transport within the liquid metal electrodes.

Generally, liquid metal batteries can avoid the head-aching issue of dendrite formation associated with solid metal deposition on the negatrode, and a high operating temperature can enhance the mobility of ions, promoting faster electrode kinetics. However, achieving high energy densities and long lifespans simultaneously in high-temperature liquid metal batteries (HTLMBs) is currently challenging due to limited materials compatibility. The corrosive nature of certain molten metals and salts can degrade or react with container materials. Thus, careful selection of compatible materials is essential to ensure long-term stability, prevent leakage, and avoid contamination.

In comparison with Li, Na has a lower melting temperature, T_m = 97.8 °C, enabling the operation of a liquid sodium battery at a lower working temperature with appropriate design. For instance, a sodium- $NiCl_2$ battery can function within the range of 270-350 °C. This battery design incorporates a solid-state β-Al_2O_3 membrane and molten $NaAlCl_4$ (T_m = 157 °C) saturated with sodium chloride (NaCl) as the electrolyte, as depicted in Fig. 13. This type of battery is known as ZEBRA batteries, developed by Coetzer in 1985.[100] The electrode reactions are shown below.

Positrode: $NiCl_2 + 2Na^+ + 2e^- = Ni + 2NaCl$ Equation (18)

Negatrode: $2Na = 2Na^+ + 2e^-$ Equation (19)

Another example of a liquid Na battery is the sodium-oxygen battery operating at 170 °C, as recently reported by Zhu et al.[32] Similar to the ZEBRA battery, this system utilized a β-alumina membrane in conjunction with $NaNO_3/KNO_3/CsNO_3$ eutectic salt as an electrolyte. The positrode consisted of Ni powder in a stainless-steel mesh, while liquid Na served as the negatrode. Through ^{18}O-labeling experiments and the discharge of Na-Ar cells, the discharge reaction was demonstrated through the electrochemical reduction as depicted below:

Positrode: $2Na^+ + NaN^{16}O_3 + 2e^- \rightarrow NaN^{16}O_2 + Na_2{}^{16}O$ step (1), Equation (20)

$Na_2{}^{16}O + 1/2\ {}^{36}O_2 \rightarrow Na_2{}^{16/18}O_2$ step (2), Equation (21)

$NaN^{16}O_2 + 1/2\ {}^{36}O_2 \rightarrow NaN^{16/18}O_3$ step (3), Equation (22)

Overall positrode reaction: $2Na^+ + {}^{36}O_2 + 2e^- \xrightarrow{N^{16}O_3^-} Na_2{}^{16/18}O_2$ Equation (23)

Negatrode: $2Na \rightarrow 2Na^{+} + 2e^{-}$ Equation (24)

Liquid Na deposition in this battery avoids the formation of dendrites that are commonly associated with solid sodium deposition in traditional batteries. When discharged at 443 K, this battery exhibited stable discharge voltages ranging from 1.9 to 2.1 V, even at high rates of up to 10 mA cm^{-2}_{geo}. The stable interface between liquid Na and β-Al_2O_3 offers advantages compared to molten-salt Li-O_2 batteries (see Fig. 14).[32] Such molten-salt Na-O_2 batteries demonstrated remarkable performance, including high energy density (33 mW h cm^{-2} $_{geo}$), power densities (19 mWcm^{-2} $_{geo}$), and stable cycling (400 cycles, 0.5 mA h cm^{-2} $_{geo}$ at 5 mA cm^{-2} $_{geo}$, with no capacity loss).

Benefiting from the low melting temperature of the eutectic salt (154 °C) composed of $NaNO_3$ (26.4 wt%), KNO_3 (27.3 wt%), and $CsNO_3$ (46.3 wt%), this high-performance liquid sodium battery can operate at 170°C. Remarkably, this temperature is lower than that of the well-known low-temperature molten salt (the eutectic temperature for $NaNO_3$ (50 mol%):KNO_3 (50 mol%) mixture is 222 °C) commonly employed for heat transfer and storage in various CSP.[101-103]

In addition to MS batteries, MS supercapacitors also deserve attentions. Recently, by using mixed $AlCl_3$-NaCl-LiCl (the melting point is 82 °C for a molar ratio of 0.6 : 0.2 : 0.2,) as electrolyte in a symmetrical cell configuration with commercial activated carbon as electrodes, Wang et al. reported pseudo-supercapacitors with very satisfactory specific energy density of 50.4 W h kg^{-1}, power capability of 1.1 kW g^{-1}, and a cycle life of 10000 cycles with 99.8 % capacity retention.[34] Benefiting from the low T_m of the mixed salt, the working temperature of the supercapacitor can be lower than 150 °C. The activated carbon, with a specific area of 2070 cm^2 g^{-1}, exhibits a cell capacitance of 73 F g^{-1} at 100 °C and 107 F g^{-1} at 175 °C.

The energy storage process follows a combined physisorption-chemisorption mechanism, attributed to the unique properties of the MS electrolyte confined in the nanopores of the electrode. The faradaic reaction is likely to occur through anion intercalation as shown below:

$C_n + AlCl_4^- \leftrightarrow C_n[AlCl_4^-] + e^-$ Equation (25)

Here, n is the molar ratio of carbon atoms to intercalated anions, a parameter dependent on factors such as pore structure and electrode potential.

Reaction (25) was confirmed by the CVs and GCDs of this molten salt supercapacitor showing two stages of capacitive dis-/charging. As illustrated in Fig. 15, at low cell voltages between E_1 (usually 0 V) and E_2, the EDL capacitance is dominant, whilst the Faradaic mechanism is invoked when the voltage increases to the range between E_2 and E_3. In the literature, such capacitive Faradic storage is termed as pseudocapacitance to differentiate it from the EDL capacitance. However, pseudocapacitance is also used to describe reversible electrochemical adsorption and desorption processes on electrode which are often Nernstian in nature. As a result, unnecessary confusions have been created when it comes to compare the performances between batteries and supercapacitors.[87] Instead of pseudocapacitance, Faraday capacitance is used in Fig. 15 to avoid confusion. Because of this additional Faraday capacitance, the overall specific capacitance of the activated carbon was significantly higher when using the $AlCl_3$-NaCl-LiCl electrolyte (419 F g^{-1} at 125 °C) compared to other non-aqueous electrolytes (typically smaller than 150 F g^{-1}). This indicates that the MS electrolyte plays a crucial role in promoting the energy density and overall performance of supercapacitors.

The provided examples effectively illustrate the application of MS electrolytes in rechargeable batteries and supercapacitors, yielding promising results. The distinctive advantages of MSs, including high ionic conductivity, robust chemical and thermal stability, a broad operating temperature window, wide electrochemical stability, suitability for high-energy-density systems, and cost-effectiveness, underscore their significant potential in developing competitive and practical EES devices for diverse market applications.

In fact, Na-$NiCl_2$ ZEBRA batteries mentioned above is, after 38 years, a quite mature technology, which are considered one of the most important electrochemical devices for stationary electrical energy storage applications due to its advantages with respect to safety, reliability, good cycle life (5000 cycles) and calendar life (over 10 years), and its materials are abundant and relatively easily sourced elements (Ni, Fe, Al, Na). MES-DEA believe that the selling price would be \$240 kWh^{-1} in low volume production (10000 units). At 100000 units per year it is projected that the price would fall to \$109 kWh^{-1}.[26]

The open-circuit voltage (OCV) is 2.58 V at 300 °C, and individual modules can achieve a OCV from 24 V to 1000 V. It has high specific energy (90-120 W h kg^{-1}) and high specific power (~ 150 W kg^{-1}) as shown in Fig. 16. While the battery is being used at between 270 °C and 350 °C, no energy penalty will be caused since the internal resistance of the battery coverts resistive losses to heat with 100 % efficiency. In addition, it is zero maintenance, no emissions under any condition, lightweight (40 % of lead acid batteries), and is not affected by external temperature. As an extremely robust and rugged battery capable of being used in demanding and harsh environments, Na-$NiCl_2$ ZEBRA is marketed by Rolls-Royce for demanding marine applications, including stand-by power in military submarines and surface vessels.[26, 104]

The global demand for batteries is projected a surge of approximately 30 percent, reaching nearly 4,500 Gigawatt-hours (GWh) annually by 2030. Currently, the electric vehicle (EV) industry dominates the total battery production capacity.[104]

Despite OPEL's successful demonstration of the electric car Astra Impuls equipped with two Na-$NiCl_2$ ZEBRA batteries in the 1990s (284 V, 25.9 kWh, charging in 6.5 hours and 10 hours offering 100 km and 150 km drive.[105] ZEBRA batteries primarily find application in stationary electrical energy storage. This, however, constitutes only a fraction of the total battery production capacity.

The high operation temperature of the Na- $NiCl_2$ ZEBRA battery poses a key challenge for its widespread use in EVs, as implementing a robust thermal control system to ensure safe operation at 300 °C remains an open challenge. Nevertheless, given the anticipation of substantial market growth and potential supply shortages for existing technologies, ZEBRA batteries could become applicable for a variety of broad applications and secure a position in the market if further cost reductions and performance improvements are achieved.[104]

As depicted in Fig. 17, 39 % of the total battery cost is attributed to cell materials, which include BASE, Ni, halide salts, etc. Notably, within the cell material cost, Ni alone constitutes 63 %, equivalent to approximately 25 % of the overall battery cost. Consequently, there is a strong interest in substituting Ni in the Na-$NiCl_2$ ZEBRA battery with more abundant and cost-effective materials. For example, Lu et al. proposed and demonstrated a novel Na-$ZnCl_2$ battery with excellent cyclability at an operating temperature of 280 °C. By

replacing the major positrode component Ni ($18.6 kg^{-1}) with Zn ($2.1 kg^{-1}), a reduction of 46 % and 20 % in cell material and overall battery costs can be achieved, respectively.[106]

The performance of Na-$NiCl_2$ batteries is constrained by the characteristics of the Ni/$NiCl_2$ couple at the positrode,[106-109] which exhibits relatively high impedance, playing a crucial role in the resistance and weight of the cell. Prakash et al. experimentally proved that the formation of a poorly conducting $NiCl_2$ layer during charging restricts the area capacity in the positrode.[108] During discharging, the formation of solid NaCl tends to cover the electrode surface, resulting in elevated resistance, thereby limiting both energy and power characteristics. It was shown that by controlling the morphology of the positrode, such kinetic issues can be significantly improved.[108] Another issue with the positrode in ZEBRA batteries, as shown in Fig. 18, is its high sensitivity to over discharge, causing irreversible loss of capacity, whilst over charge can also cause problems at the positrode, although it may be better controlled.[109]

This leads to the hypothesis that substantial enhancements in battery performance can be achieved through a redesign of the cell configuration to eliminate the problematic the Ni/$NiCl_2$ positrode. An innovative proposal involves replacing the Ni/$NiCl_2$ positrode and posilyte with an activated carbon electrode in a molten $AlCl_3$-NaCl-LiCl system.[34] Building upon this concept, the Na-$NiCl_2$ battery can be transformed into a supercapattery, with the capacitive electrode serving as the positrode. The integration of a carbon positrode not only contributes to cost reduction and a lower operation temperature but also facilitates rapid charge transfer, mitigating issues associated with electrolyte composition changes and heterogeneous 'non-Nernstian' charge/discharge behaviour linked to the Ni/$NiCl_2$ couple at the positrode (as depicted in the Fig. 18).

4. Prospects of supercapatteries and a hypothetical molten salt Na-AC supercapattery

In this part, we envision a tubular MS supercapattery design inspired by the configuration of ZEBRA batteries. The system comprises activated carbon serving as the positrode (capacitive) and liquid sodium as the negatrode (battery-like). The electrolyte consists of a β-Al_2O_3 membrane interfacing with molten $AlCl_3$-NaCl-LiCl. The practical viability of this innovative design has been discussed above by reviewing existing promising MS batteries and MS supercapacitor technologies. This section delves into the theoretical feasibility through discussions on thermodynamic calculations.

Due to the increasing demand for replacing fossil fuels with renewables, especially to a significant extent, high specific energy, or energy density, EES technologies are crucial to compete with fossil fuels from an economic perspective. Fossil fuel typically contain 10-20 kW h kg^{-1} in specific energy, as derived from enthalpy changes (ΔH^o) of combustion reactions, such as carbon (coal) and methane (natural gas) in Equation (26) and (27):

$$C + O_2 = CO_2 \quad \Delta H^o\ (298\ K) = -393.51\ kJ \qquad \text{Equation (26)}$$

$$CH_4 + 2O_2 = CO_2 + 2H_2O\ \ \Delta H^o\ (298\ K) = -980.56\ kJ \qquad \text{Equation (27)}$$

The specific enthalpy, ΔH^o_{sp}, of carbon and methane combustion in W h kg^{-1} can be derived using the following equation:

$$\Delta H^o_{sp} = \frac{\Delta H^o}{\sum \gamma_{r,j} M_{r,j}} = \frac{\Delta H^o}{\sum \gamma_{p,j} M_{p,j}} \qquad \text{Equation (28)}$$

where $M_{r,j}$ and $M_{p,j}$ represent the formula masses, and $r_{r,j}$ and $r_{p,j}$ are stoichiometric coefficients of the j^{th} reactant and product, respectively. Since 1 W h =3600 J, the calculated specific enthalpy values are −2.48 and −3.41 kW h kg^{-1} for carbon and methane, respectively. However, because O_2 is a gas and can be obtained from air, it is practically reasonable to ignore the O_2 mass in the calculation, leading to −9.11 and −17.06 kW h kg^{-1} for carbon and methane, respectively.

The enthalpy change can be directly linked to the heat that is needed for warming a house, for example. However, for the power needed to drive a car, for instance, not all the enthalpy change can be converted to work due to entropy loss. The portion of the enthalpy change available for doing work is the Gibbs free energy change, ΔG^o, which is linked to the enthalpy and entropy changes, ΔS^o, by the following equation:

$$\Delta G = \Delta H - T\Delta S \qquad \text{Equation (29)}$$

The specific Gibbs free energy changes of reactions (26) and (27) can then be calculated, taking into account only the mass of the fuel, to be −9.13 and −14.20 kW h kg^{-1}, respectively. Similar calculations can be applied to battery reactions, but in such cases, it is the Gibbs free energy change, i.e. ΔG^o, that matters. Similar to Equation (28), specific Gibbs free energy, ΔG^o_{sp}, can be expressed as:

$$\Delta G_{\mathrm{sp}}^{\mathrm{o}} = \frac{\Delta G^{\mathrm{o}}}{\sum \gamma_{\mathrm{r,j}} M_{\mathrm{r,j}}} = \frac{\Delta G^{\mathrm{o}}}{\sum \gamma_{\mathrm{p,j}} M_{\mathrm{p,j}}} \quad \text{Equation (30)}$$

Thus, for the lead-acid battery, $\Delta G_{\mathrm{sp}}^{\mathrm{o}} = -167.34$ W h kg^{-1}and for the alkaline Zn-MnO_2 battery $\Delta G_{\mathrm{sp}}^{\mathrm{o}} = -306.10$ W h kg^{-1}.[36] In reality, due to mainly kinetic causes, the specific energy of the lead-acid battery is only 30-40 W h kg^{-1}, while that of the alkaline Zn-MnO_2 battery reaches up to 150 W h kg^{-1}.[110, 111] Although the Li-O_2 battery can reach a very high value of $\Delta G_{\mathrm{sp}}^{\mathrm{o}} = -5216.48$ W h kg^{-1},[36] this new device still remains in research and development due to various challenges such as fundamental understanding, materials stability and device engineering.[112]

Not all battery reactions can be found in available thermodynamic databases, but it is still possible to derive their $\Delta G_{\mathrm{sp}}^{\mathrm{o}}$ values from the discharging performance of batteries. When you have an idea of the discharging cell voltage for a battery, U_{cell}, it can then be linked to ΔG^{o} by Equation (31) below:

$$\Delta G^{\mathrm{o}} = -nFU_{\mathrm{cell}} \quad \text{Equation (31)}$$

The cell specific energy can then be calculated according to Equation (30). The theoretical specific discharging capacity, $Q_{\mathrm{sp,cell}}$, for the cell reaction can be calculated according to the equation below:

$$Q_{\mathrm{sp,cell}} = \frac{nF}{\sum \gamma_{\mathrm{r,j}} M_{\mathrm{r,j}}} = \frac{nF}{\sum \gamma_{\mathrm{p,j}} M_{\mathrm{p,j}}} \quad \text{Equation (32)}$$

Based on the discussion above, MS batteries and MS capacitors have been extensively researched, providing a solid foundation and confidence for the development of MS supercapatteries. Here, a MS supercapattery with a tubular design similar to that of the ZEBRA battery is hypothesized, with activated carbon as the positrode and liquid sodium as the negatrode. The electrolyte is a β-Al_2O_3 membrane|$AlCl_3$-NaCl-LiCl.

Theoretically, $Q_{\mathrm{sp}} = nF/M$ where M is the formula mass, and it can be calculated to be 1340 C g^{-1} for carbon. Experimentally, the AC electrode in MS supercapacitors can achieve, as mentioned above. For a liquid sodium negatrode, $Q_{\mathrm{sp,Na}} = nF/M_{\mathrm{Na}} = 4195$ C g^{-1} ($F = 96485$ C mol^{-1}, $M_{\mathrm{Na}} = 22.990$ g mol^{-1}, $n = 1$). For the activated carbon positrode with $C_{\mathrm{sp,C}} = 400$ F g^{-1} and the U_{max} of 3.5 V, the U_{min} of 0.5 V.

Following Equation (13), the weight ratio of AC and sodium can be obtained by:

$$\frac{m_{\mathrm{C}}}{m_{\mathrm{Na}}} = \frac{Q_{\mathrm{sp,Na}}}{C_{\mathrm{sp,C}}\Delta E} = \frac{4195}{400\times(3.5-0.5)} = 3.5 \qquad \text{Equation (33)}$$

This implies that the mass of the liquid negatrode is not negligible. Because the cell still behaves in a capacitive way, as shown in Fig. 9 (c), it is practically appropriate to estimate an apparent specific capacitance of the sodium electrode. Since the potential change of the sodium negatrode is smaller than 500 mV along the potential plateau, the apparent specific capacitance $C_{\mathrm{sp,Na}}$ should be larger than 4195/0.5 = 8390 F g^{-1}. The specific energy of such a sodium-carbon supercapattery can be calculated using Equation (34):

$$\frac{1}{C_{\mathrm{cell}}} = \frac{1}{m_{\mathrm{C}}C_{\mathrm{sp,C}}} + \frac{1}{m_{\mathrm{Na}}C_{\mathrm{sp,Na}}} \qquad \text{Equation (34)}$$

It can then be derived that the specific cell capacitance is $C_{\mathrm{sp,cell}} = \frac{C_{\mathrm{cell}}}{m_{\mathrm{C}}+m_{\mathrm{Na}}} = \frac{3.5\times400\times8390}{(3.5\times400+8390)\times(3.5+1)} = 267$ F g^{-1}. Thus, from Equation (10), the specific energy of the sodium-activated carbon supercapattery can be calculated to be $W_{\mathrm{sp}} = \frac{C_{\mathrm{sp,cell}}}{2}(U_{\mathrm{max}}^2 - U_{\mathrm{min}}^2) = \frac{1}{2}\times 267 \times (3.5^2 - 0.5^2) = 1602$ J g^{-1}= 445 W h kg^{-1}-AM (AM is the total active mass on both electrodes).

For a liquid lithium negatrode, $Q_{\mathrm{sp,Li}} = nF/M_{\mathrm{Li}}$ = 13900 C g^{-1} (F = 96485 C mol^{-1}, M_{Li} = 6.941 g mol^{-1}, n = 1). For the activated carbon positrode with $C_{\mathrm{sp,C}}$ = 400 F g^{-1} and the U_{max} of 4.5 V, the U_{min} of 0.5 V, $\frac{m_{\mathrm{C}}}{m_{\mathrm{Li}}} = 11.6$. As a result, the total mass of lithium metal used to build the supercapattery is negligible compared to that of the activated carbon. The specific energy of such a lithium-carbon supercapattery can be calculated using Equation (34), in which $C_{\mathrm{cell}} \approx m_{\mathrm{C}}C_{\mathrm{sp,C}} = 400$ F g^{-1}. Thus, $W_{\mathrm{sp}} = \frac{C_{\mathrm{sp,cell}}}{2}(U_{\mathrm{max}}^2 - U_{\mathrm{min}}^2) = \frac{1}{2}\times 400 \times (4.5^2 - 0.5^2) = 4000$ J g^{-1} = 1111 W h kg^{-1}-AM (AM is the total active mass on both electrodes).

In this design, the proposed supercapattery is practically possible to outperform the commercial Li-ion battery, the best performance of which has a W_{sp} of 250 W h kg^{-1}-cell.

While MS electrolytes have not been demonstrated in supercapattery, an emerging EES device, insights from existing research on MS batteries and supercapacitors can provide initial considerations for the development of MS supercapattery. This is because (1) a supercapattery essentially represents a combination of battery and supercapacitor technologies; (2) the commercial battery and capacitor are similar in looking, coins type,

tubular design, modules etc; (3) mature industrial process has been developed for the assembling ZEBRA batteries, which provides viability for future MS supercapatteries to be integrated into the existing technology. Therefore, MS supercapattery derived from, but potentially better than supercapacitor and battery in aspects of commercial attractiveness and potential fossil-comparable energy capacity, is a promising candidate for next generation energy storage technology.

Author Contributions

Yu Yu and Yuhan Zhang were responsible for drafting the manuscript, with Yu Yu focusing on the main body and Yuhan Zhang on the introduction. Han Wang actively participated in the initial discussions and the construction of the manuscript. George Z. Chen played a crucial role in supervising, engaging in discussions, and revising the manuscript.

Conflicts of interest

There are no conflicts to declare.

Acknowledge

We would like to express our appreciation for the current and past financial supports from the Innovate UK (Smart Grants, 10017140), E.ON AG (Energy Storage Award 2007), Royal Society (Braine Mercer Feasibility Award, 2006), and EPSRC (EP/J000582/1, GR/R68078).

References

1. H. MacPherson, *Nucl. Sci. Eng.*, **90**, 374 (1985).

2. J. Uhlíř, *J. Nucl. Mater.*, **360**, 6 (2007).

3. B. C. Kelleher, Ph.D. Thesis, The University of Wisconsin-Madison, Madison, the United States (2015).

4. https://www.daretothink.org/europe-evols-molten-salt-fast-reactor/ referred on 11 Dec, 2023.

5. https://world-nuclear.org/information-library/current-and-future-generation/molten-salt-reactors.aspx referred on 11 Dec, 2023.

6. https://www.neimagazine.com/news/newschinas-experimental-molten-salt-reactor-receives-licence-10952226 referred on 11 Dec 2023.

7. G. Z. Chen, D. J. Fray, and T. W. Farthing, *Nature*, **407**, 361 (2000).

8. E.-Y. Choi, and S. M. Jeong, *Prog. Nat. Sci.: Mater. Int.*, **25**, 572 (2015).

9. A. Stevenson, D. Hu, and G. Z. Chen, *ECS Trans.*, **64**, 333 (2014).

10. R. W. Bradshaw, D. B. Dawson, W. De La Rosa, R. Gilbert, S. H. Goods, M. J. Hale, P. Jacobs, S. A. Jones, G. J. Kolb, and J. E. Pacheco, Final test and evaluation results from the solar two project, the United States Janurary (2002).

11. A. Bonk, M. Braun, V. A. Sötz, and T. Bauer, *Appl. Energy*, **262**, 114535-1 (2020).

12. P. Sabharwall, and S.-J. Yoon, Nuclear hybrid energy system: Molten salt energy storage (summer report 2013), the United States, (2013).

13. X. Xu, X. Wang, P. Li, Y. Li, Q. Hao, B. Xiao, H. Elsentriecy, and D. Gervasio, *J. Sol. Energy Eng.*, **140**, 051011-1 (2018).

14. K. Borowiec, A. Wysocki, S. Shaner, M. S. Greenwood, and M. Ellis, *J. Energy Resour. Technol.*, **142**, 042006-1 (2019).

15. D. Cocco, and F. Serra, *Energy*, **81**, 526 (2015).

16. R. Roper, M. Harkema, P. Sabharwall, C. Riddle, B. Chisholm, B. Day, and P. Marotta, *Ann. Nucl. Energy*, **169**, 108924-1 (2022).

17. J. M. Bergthorson, *Prog. Energy Combust. Sci.*, **68**, 169 (2018).

18. G. Z. Chen, Application for the Royal Society 2007 Brian Mercer Feasibility Award (2006).

19. S. Licht, B. Wang, S. Ghosh, H. Ayub, D. Jiang, and J. Ganley, *J. Phys. Chem. Lett.*, **1**, 2363 (2010).

20. H. V. Ijije, R. C. Lawrence, and G. Z. Chen, *RSC Adv.*, **4**, 35808 (2014).

21. H. V. Ijije, C. Sun, and G. Z. Chen, *Carbon*, **73**, 163 (2014).

22. D. Ji, Z. Li, W. Li, D. Yuan, Y. Wang, Y. Yu, and H. Wu, *Int. J. Hydrog. Energy*, **44**, 5082 (2019).

23. J. B. Goodenough, *J. Solid State Electrochem.*, **16**, 2019 (2012).

24. J. Coetzer, *J. Power Sources*, **18**, 377 (1986).

25. H. Böhm, and G. Beyermann, *J. Power Sources*, **84**, 270 (1999).

26. http://www.meridian-int-res.com/Projects/Zebra_Pages.pdf referred on 20 Dec, 2023.

27. D. J. Bradwell, H. Kim, A. H. C. Sirk, and D. R. Sadoway, *J. Am. Chem. Soc.*, **134**, 1895 (2012).

28. H. Kim, D. A. Boysen, T. Ouchi, and D. R. Sadoway, *J. Power Sources*, **241**, 239 (2013).

29. Y. Song, S. Jiao, J. Tu, J. Wang, Y. Liu, H. Jiao, X. Mao, Z. Guo, and D. J. Fray, *J. Mater. Chem. A* **5**, 1282 (2017).

30. H. Yin, B. Chung, F. Chen, T. Ouchi, J. Zhao, N. Tanaka, and D. R. Sadoway, *Nature Energy*, **3**, 127 (2018).

31. S. Licht, B. Cui, J. Stuart, B. Wang, and J. Lau, *Energy Environ. Sci.*, **6**, 3646 (2013).

32. Y. G. Zhu, G. Leverick, A. Accogli, K. Gordiz, Y. Zhang, and Y. Shao-Horn, *Energy Environ. Sci.*, **15**, 4636 (2022).

33. D. W. Kirk, and J. W. Graydon, *ECS Trans.*, **53**, 27 (2013).

34. K. Wang, Z. Chen, K. Liu, C. Yang, H. Zhang, Y. Wu, Y. Long, H. Liu, Y. Jin, and M. Li, *Energy Environ. Sci.*, **15**, 5229 (2022).

35. B. Akinwolemiwa, C. Peng, and G. Z. Chen, *J. Electrochem. Soc.*, **162**, A5054 (2015).

36. G. Z. Chen, *Int. Mater. Rev.*, **62**, 173 (2017).

37. W. Shimizu, S. Makino, K. Takahashi, N. Imanishi, and W. Sugimoto, *J. Power Sources*, **241**, 572 (2013).

38. L. Yu, and G. Z. Chen, *Faraday Discuss.*, **190**, 231 (2016).

39. D. Hu, C. Peng, and G. Z. Chen, *ACS Nano*, **4**, 4274 (2010).

40. S. Makino, Y. Shinohara, T. Ban, W. Shimizu, K. Takahashi, N. Imanishi, and W. Sugimoto, *RSC Adv.*, **2**, 12144 (2012).

41. R. Kötz, and M. Carlen, *Electrochim. Acta*, **45**, 2483 (2000).

42. G. Z. Chen, *Prog. Nat. Sci.: Mater. Int.*, **23**, 245 (2013).

43. J. H. Chae, K. C. Ng, and G. Z. Chen, *Proc. Inst. Mech. Eng. A*, **224**, 479 (2010).

44. S. W. Zhang, and G. Z. Chen, *Energy Mater.*, **3**, 186 (2008).

45. A. J. Bard, and L. R. Faulkner, Electrochemical methods: Fundamentals and applications, John Wiley & Sons, the United States 228 (2001).

46. L. Guan, L. Yu, and G. Z. Chen, *Electrochim. Acta*, **206**, 464 (2016).

47. H. Zhang, G. Cao, and Y. Yang, *Energy Environ. Sci.*, **2**, 932 (2009).

48. H. Pan, J. Li, and Y. Feng, *Nanoscale Res. Lett.*, **5**, 654 (2010).

49. T.-S. Hyun, H. L. Tuller, D.-Y. Youn, H.-G. Kim, and I.-D. Kim, *J. Mater. Chem.*, **20**, 9172 (2010).

50. L. Dai, D. W. Chang, J. B. Baek, and W. Lu, *Small*, **8**, 1130 (2012).

51. B. E. Conway, and E. Gileadi, *Trans. Faraday Soc.*, **58**, 2493 (1962).

52. J. M. Hale, and R. Greef, *Electrochim. Acta*, **12**, 1409 (1967).

53. S. Trasatti, and G. Buzzanca, *J. Electroanal. Chem. Interf. Electrochem.*, **29**, A1 (1971).

54. S. H. Glarum, and J. H. Marshall, *J. Electrochem. Soc.*, **134**, 2160 (1987).

55. E. M. Genies, and C. Tsintavis, *J. Electroanal. Chem. Interf. Electrochem.*, **195**, 109 (1985).

56. A. Rudge, J. Davey, I. Raistrick, S. Gottesfeld, and J. P. Ferraris, *J. Power Sources*, **47**, 89 (1994).

57. F. Masamichi, M. Tomokazu, and O. Tetsuo, *Chem. Lett.*, **5**, 875 (1976).

58. G. A. Tsirlina, S. Y. Vasil'ev, Y. E. Roginskaya, and G. G. Postovalova, *Russ. J. Electrochem.*, **35**, 1380 (1999).

59. H. Y. Lee, and J. B. Goodenough, *J. Solid State Chem.*, **144**, 220 (1999).

60. H. Y. Lee, and J. B. Goodenough, *J. Solid State Chem.*, **148**, 81 (1999).

61. B. Akinwolemiwa, and G. Z. Chen, *J. Braz. Chem. Soc.*, **29**, 960 (2018).

62. J. H. Chae, K. C. Ng, and G. Z. Chen, *Proceedings of the Institution of Mechanical Engineers, Part A: Journal of Power and Energy*, **224**, (2010).

63. B. E. Conway, *J. Electrochem. Soc.*, **138**, 1539 (1991).

64. J. H. Chae, X. Zhou, and G. Z. Chen, *Green*, **2**, 41 (2012).

65. L. Yu, and G. Z. Chen, *Electrochem. Energy Rev.*, **3**, 271 (2020).

66. L. Yu, and G. Z. Chen, *J. Power Sources*, **326**, 604 (2016).

67. V. Srinivasan, and J. W. Weidner, *J. Electrochem. Soc.*, **147**, 880 (2000).

68. X. Jin, W. Zhou, S. Zhang, and G. Z. Chen, *Small*, **3**, 1513 (2007).

69. V. J. Mane, D. B. Malavekar, S. B. Ubale, R. N. Bulakhe, I. In, and C. D. Lokhande, *Electrochim. Acta*, **335**, 135613-1 (2020).

70. Y. Hu, Y. Wu, and J. Wang, *Adv. Mater.*, **30**, 1870364-1 (2018).

71. B. Akinwolemiwa, C. Wei, Q. Yang, L. Yu, L. Xia, D. Hu, C. Peng, and G. Z. Chen, *J. Electrochem. Soc.*, **165**, A4067 (2018).

72. Q. Abbas, H. Fitzek, V. Pavlenko, and B. Gollas, *Electrochim. Acta*, **337**, 135785-1 (2020).

73. F. Yu, C. Zhang, F. Wang, Y. Gu, P. Zhang, E. R. Waclawik, A. Du, K. Ostrikov, and H. Wang, *Mater. Horiz.*, **7**, 495 (2020).

74. G. G. Amatucci, F. Badway, A. Du Pasquier, and T. Zheng, *J. Electrochem. Soc.*, **148**, A930 (2001).

75. T. Aida, K. Yamada, and M. Morita, *Electrochem. Solid-State Lett.*, **9**, A534 (2006).

76. S.-W. Woo, K. Dokko, H. Nakano, and K. Kanamura, *Electrochemistry*, **75**, 635 (2007).

77. S. Panero, E. Spila, and B. Scrosati, *J. Electroanal. Chem.*, **396**, 385 (1995).

78. D. Komatsu, T. Tomai, and I. Honma, *J. Power Sources*, **274**, 412 (2015).

79. C. J. Hung, P. Lin, and T. Y. Tseng, *J. Power Sources*, **259**, 145 (2014).

80. B. E. Conway, V. Birss, and J. Wojtowicz, *J. Power Sources*, **66**, 1 (1997).

81. S. R. Sivakkumar, J. Y. Nerkar, and A. G. Pandolfo, *Electrochim. Acta*, **55**, 3330 (2010).

82. Z. Shi, J. Zhang, J. Wang, J. Shi, and C. Wang, *Electrochim. Acta*, **153**, 476 (2015).

83. J. Xie, P. Yang, Y. Wang, T. Qi, Y. Lei, and C. M. Li, *J. Power Sources*, **401**, 213 (2018).

84. *Renew. Energy Focus*, **9**, 10 (2008).

85. S. Lalwani, A. Joshi, G. Singh, and R. K. Sharma, *Electrochim. Acta*, **328**, 135076-1 (2019).

86. N. Joseph, and A. C. Bose, *Electrochim. Acta*, **301**, 401 (2019).

87. G. Z. Chen, *Curr. Opin. Electrochem.*, **21**, 358 (2020).

88. J. Lin, Z. Zhong, H. Wang, X. Zheng, Y. Wang, J. Qi, J. Cao, W. Fei, Y. Huang, and J. Feng, *J. Power Sources*, **407**, 6 (2018).

89. S. Lin, C. Zhang, Z. Wang, S. Dai, and X. Jin, *Adv. Energy Mater.*, **7**, 1700766-1 (2017).

90. H. Wang, T. Maiyalagan, and X. Wang, *ACS Catal.*, **2**, 781 (2012).

91. T. Lin, I. W. Chen, F. Liu, C. Yang, H. Bi, F. Xu, and F. Huang, *Science*, **350**, 1508 (2015).

92. G. T.-K. Fey, Y.-C. Lin, and H.-M. Kao, *Electrochim. Acta*, **80**, 41 (2012).

93. S. W. Oh, S.-T. Myung, H. J. Bang, C. S. Yoon, K. Amine, and Y.-K. Sun, *Electrochem. Solid-State Lett.*, **12**, A181 (2009).

94. M.-Y. Cho, S.-M. Park, K.-B. Kim, J.-W. Lee, and K. C. Roh, *J. Electrochem. Sci. Technol.*, **3**, 135 (2012).

95. S. W. Oh, S.-T. Myung, S.-M. Oh, K. H. Oh, K. Amine, B. Scrosati, and Y.-K. Sun, *Adv. Mater.*, **22**, 4842 (2010).

96. Q. Guo, P. Fan, Y. Zhang, L. Guan, H. Wang, A. Croft, and G. Z. Chen, *RSC Sustainability*, **2**, 101 (2024).

97. S. Zhang, Y. Yang, L. Cheng, J. Sun, X. Wang, P. Nan, C. Xie, H. Yu, Y. Xia, B. Ge, J. Lin, L. Zhang, C. Guan, G. Xiao, C. Peng, G. Z. Chen, and J.-Q. Wang, *Energy Storage Mater.*, **35**, 142 (2021).

98. K. Wang, K. Jiang, B. Chung, T. Ouchi, P. J. Burke, D. A. Boysen, D. J. Bradwell, H. Kim, U. Muecke, and D. R. Sadoway, *Nature*, **514**, 348 (2014).

99. H. Ohtani, K. Okuda, and K. Ishida, *J. Phase Equilib.*, **16**, 416 (1995).

100. J. Coetzer, and M. M. Thackeray, U. S. Patent, 4288506 (1981).

101. M. Durth, C. Prieto, A. Rodríguez-Sánchez, D. Patiño-Rodríguez, and L. F. Cabeza, *Solar Energy*, **182**, (2019).

102. R. Benages-Vilau, T. Calvet, M. A. Cuevas-Diarte, and H. A. J. Oonk, *Phase Transitions*, **89**, (2016).

103. B. D'Aguanno, M. Karthik, A. N. Grace, and A. Floris, *Scientific Reports*, **8**, (2018).

104. M. Armand, N. Ortiz-Vitoriano, J. Olarte, A. Salazar, and R. Ferret, Salt batteries: Opportunities and applications of storage systems based on sodium nickel chloride batteries, Belgium, February (2023).

105. R. Bady, J.-W. Biermann, B. Kaufmann, and H. Hacker, European electric vehicle fleet demonstration with zebra batteries, SAE Technical Paper, March (1999).

106. X. Lu, G. Li, J. Y. Kim, J. P. Lemmon, V. L. Sprenkle, and Z. Yang, *Energy Environ. Sci.*, **6**, 1837 (2013).

107. L. Zhao, J. Zhao, Y.-S. Hu, H. Li, Z. Zhou, M. Armand, and L. Chen, *Adv. Energy Mater.*, **2**, 962 (2012).

108. J. Prakash, L. Redey, and D. R. Vissers, *J. Power Sources*, **84**, 63 (1999).

109. C.-H. Dustmann, *J. Power Sources* **127**, 85 (2004).

110. J. X. Weinert, A. F. Burke, and X. Wei, *J. Power Sources*, **172**, 938 (2007).

111. M. B. Lim, T. N. Lambert, and B. R. Chalamala, *Mater. Sci. Eng. R Rep.*, **143**, 100593-1 (2021).

112. L. Grande, E. Paillard, J. Hassoun, J.-B. Park, Y.-J. Lee, Y.-K. Sun, S. Passerini, and B. Scrosati, *Adv. Mater.*, **27**, 784 (2015).

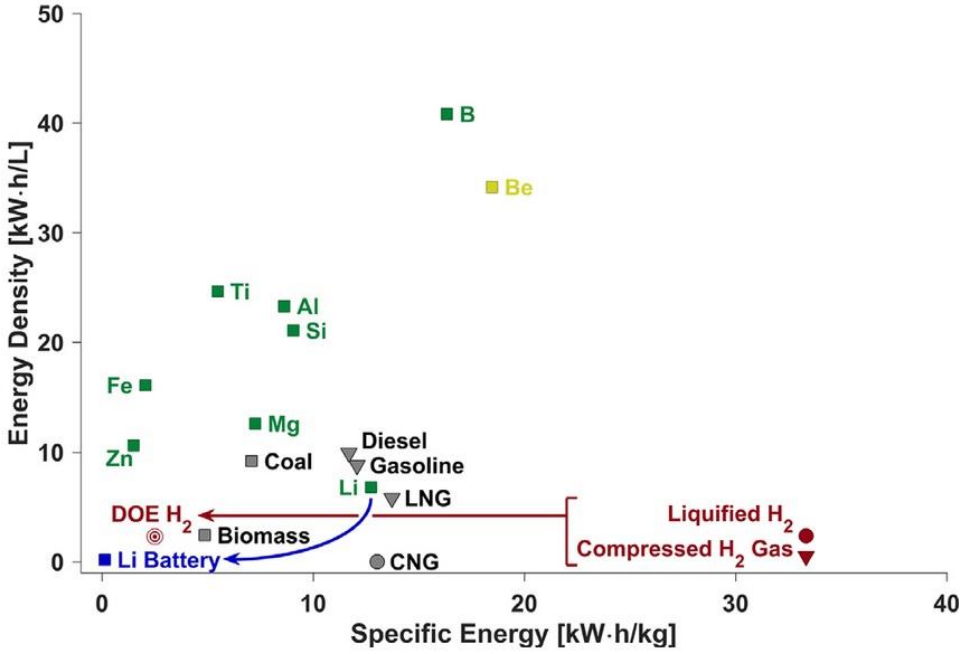

Figure 1. Comparative analysis of energy density and specific energy across metal fuels, batteries, bio-derived fuels, fossil fuels, and hydrogen.[17] The energy density and specific energy of metal fuels were determined through the standard enthalpy of formation (ΔH_f^o, 298.15 K), whereas heat values were employed for evaluating the energy density and specific energy of biofuels, fossil fuels, and hydrogen. Abbreviation used: compressed natural gas (CNG), liquefied natural gas (LNG), compressed hydrogen gas (CH_2G), liquid hydrogen (LH_2), and the energy density goal for hydrogen storage materials set by the U.S. Department of Energy (DOE H_2). (Reprinted from Ref. 17 according to the Open Access Licence CC By, Elsevier).

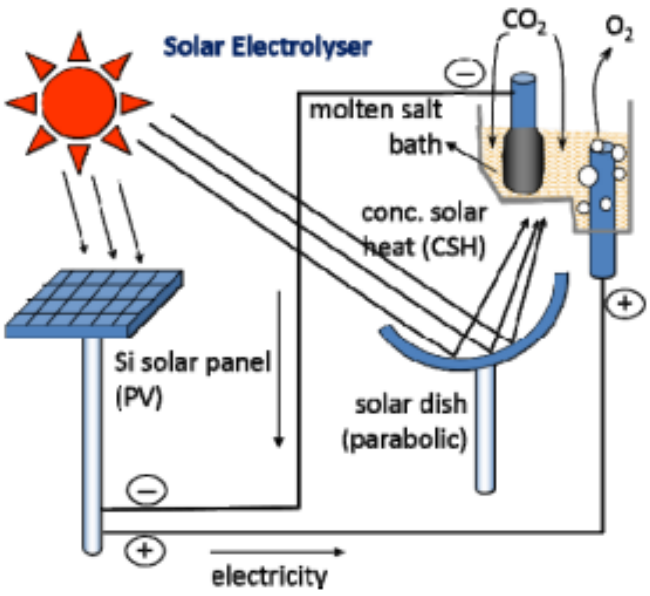

Figure 2. Schematic illustration of a molten salt electrolyser designed for carbon dioxide reduction into solid carbon.[18] The parabolic dish CSP technology heats the electrolyser, and the electrolysis is powered by the electricity generated by Si solar panels.

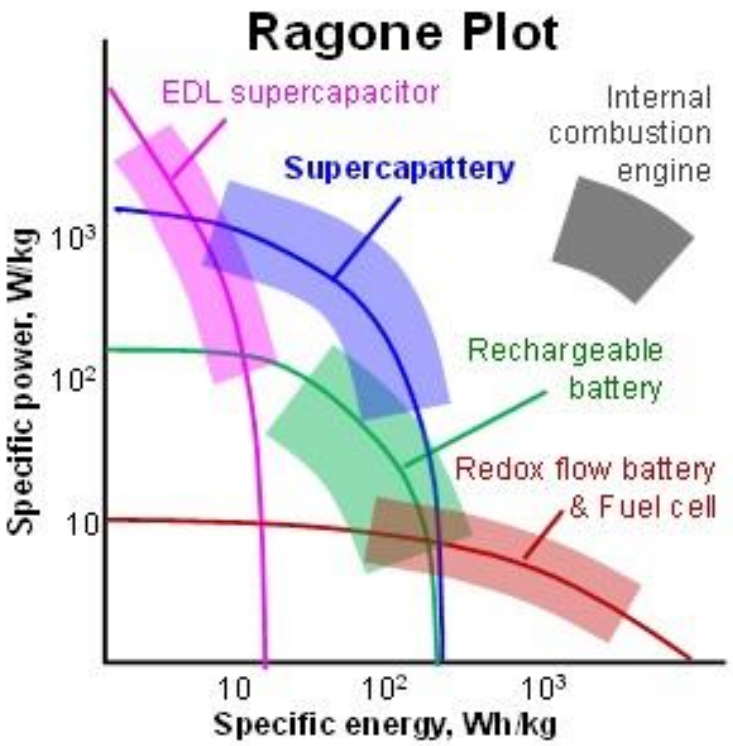

Figure 3. A schematic Ragone plot comparing the specific energy and specific power of supercapattery with other energy technologie.[36, 41] (Reprinted from Ref. 36 according to the Open Access Licence CC By, Taylor & Francis).

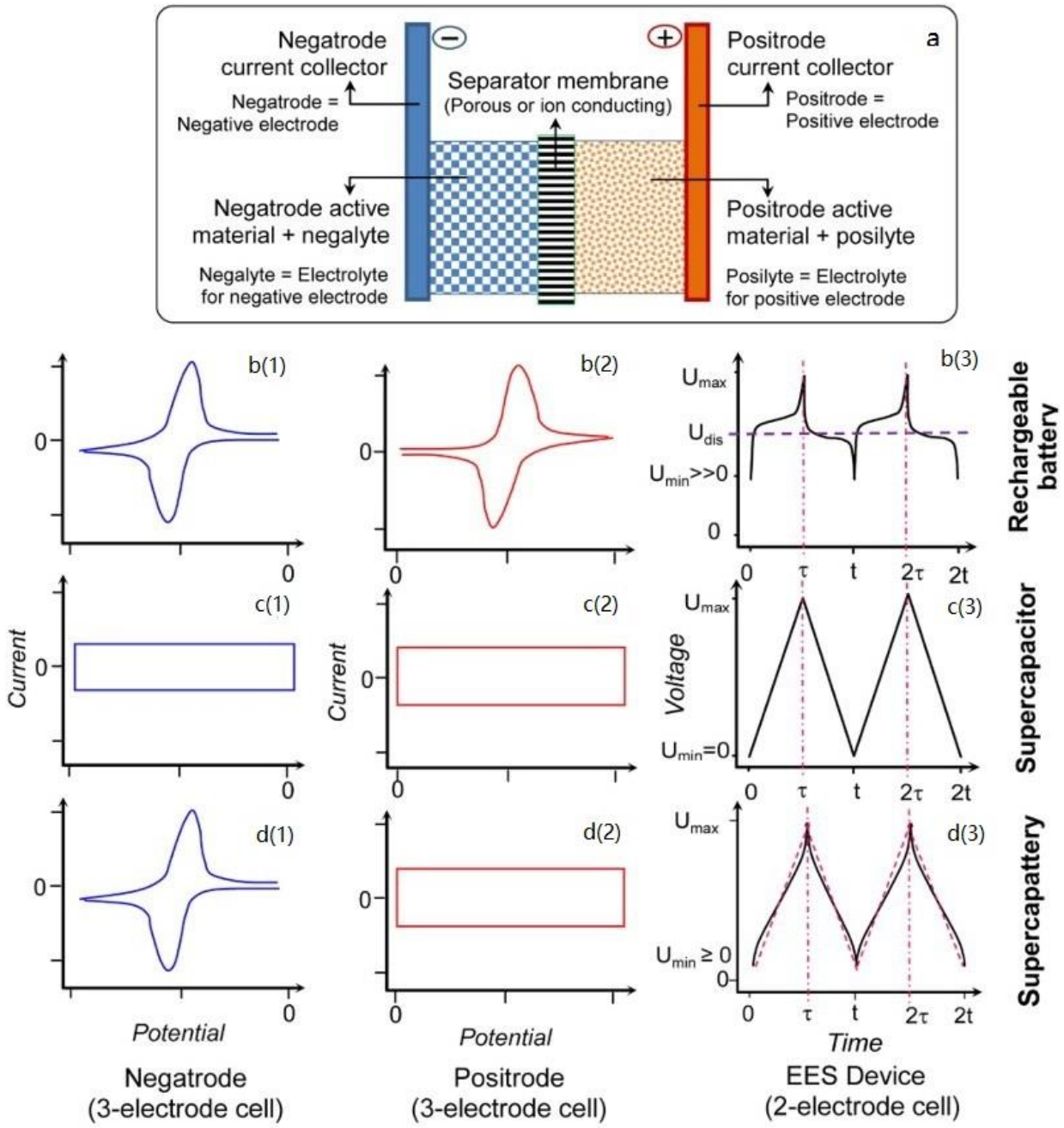

Figure 4. Schematic representations of (a) components of a typical EES device. Three-electrode cell CVs for the negatrode (1) and positrode (2), and GCDs (3) for the two-electrode cell in (b) rechargeable battery, (c) supercapacitor, and (d) supercapattery. [35, 36, 39, 42] (Redrawn and reprinted from Ref. 36 according to the Open Access Licence CC By, Taylor & Francis).

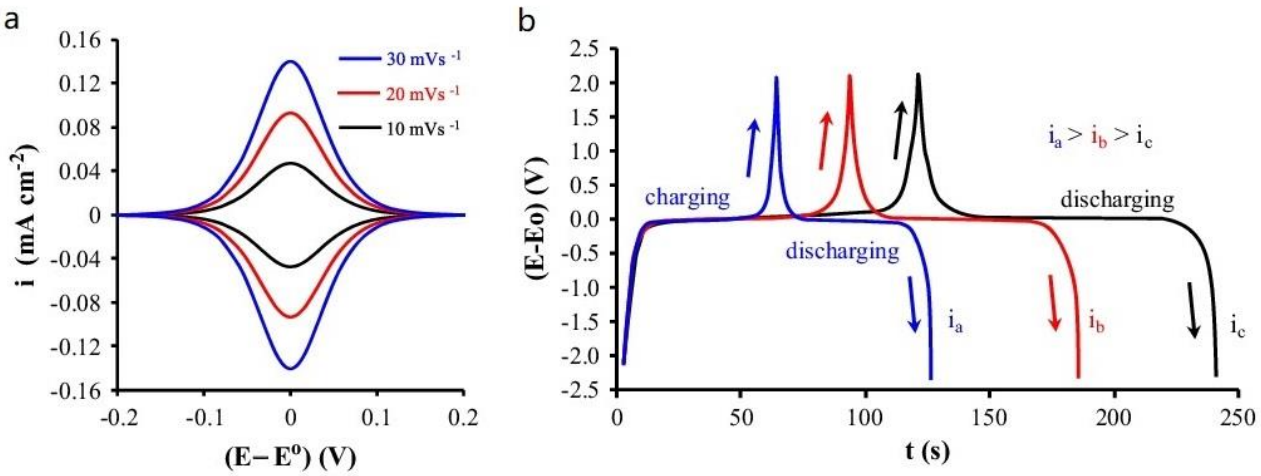

Figure 5. (a) CVs recorded at indicated potential scan rates, and (b) GCDs obtained at indicated constant currents ($i_a > i_b > i_c$) for a reversible Faradaic reaction involving localised electron transfer to and from isolated redox sites on the electrode.[36, 42-44] (Reprinted from Ref. 42 with permission from Elsevier).

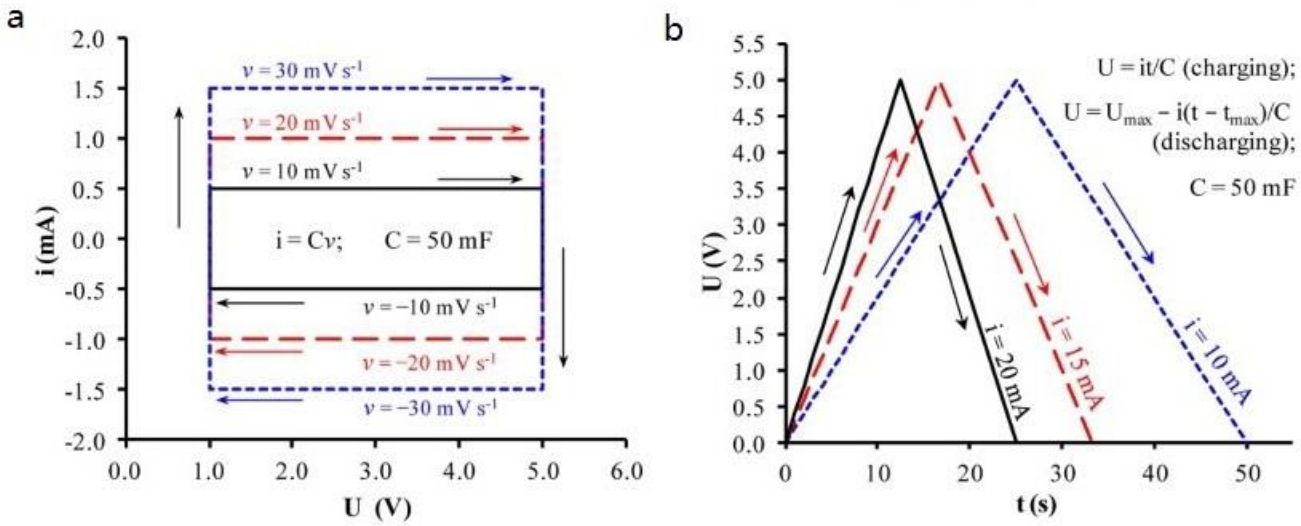

Figure 6. (a) CVs recorded at indicated voltage scan rates, and (b) GCDs obtained at indicated constant currents, derived from Equation (8), for a 50 mF capacitor with U_{max} = 5 V. In the GCDs in (b), t_{max} = $U_{max}C/i$.[36,42] (Reprinted from Ref. 36 according to the Open Access Licence CC By, Taylor & Francis).

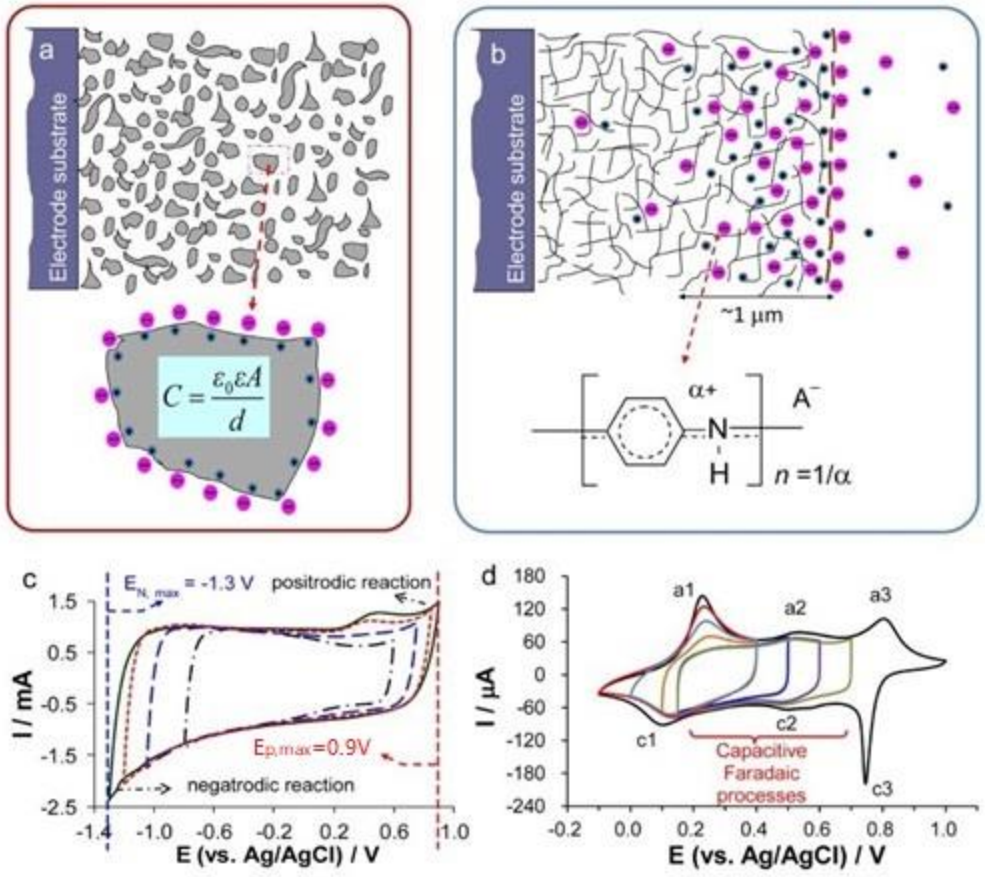

Figure 7. (a, b) Cross-sectional schematic views of (a) a carbon powder electrode and (b) a polyaniline electrode. The enlarged view below (a) illustrates charge storage on a single carbon particle through ion adsorption at the carbon|electrolyte interface, representing the EDL capacitance. (c, d) CVs of (c) activated carbon (2.5 mg) in 0.3 mol L^{-1} K_2SO_4 at 5 mV s^{-1} and (d) electrodeposited polyaniline (10 mC) in 1.0 mol L^{-1} HCl at 20 mV s^{-1} across different potential ranges.[36,42] (Reprinted from Ref. 36 according to the Open Access Licence CC By, Taylor & Francis).

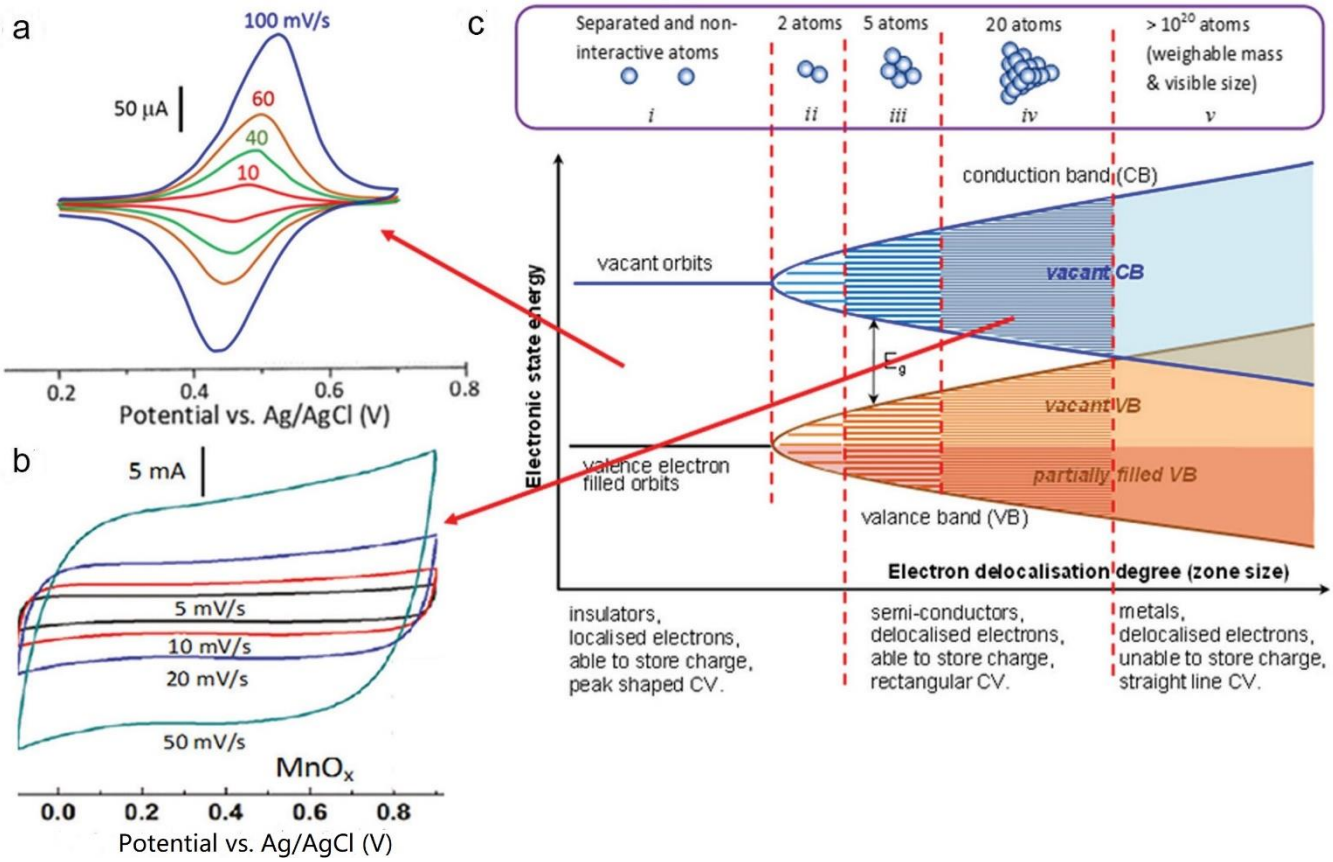

Figure 8. Charge storage mechanisms: (a) Non-capacitive Faradaic or Nernstian mechanism of ferrocene-containing inactive polymer-coated electrode in aqueous electrolyte; (b) Capacitive Faradaic mechanism of MnO_x-coated electrode in aqueous electrolyte; (c) Band model for the description of charge storage mechanisms.[36,61] (Reprinted from Ref. 61 according to the Open Access Licence CC By, Brazilian Society of Chemistry).

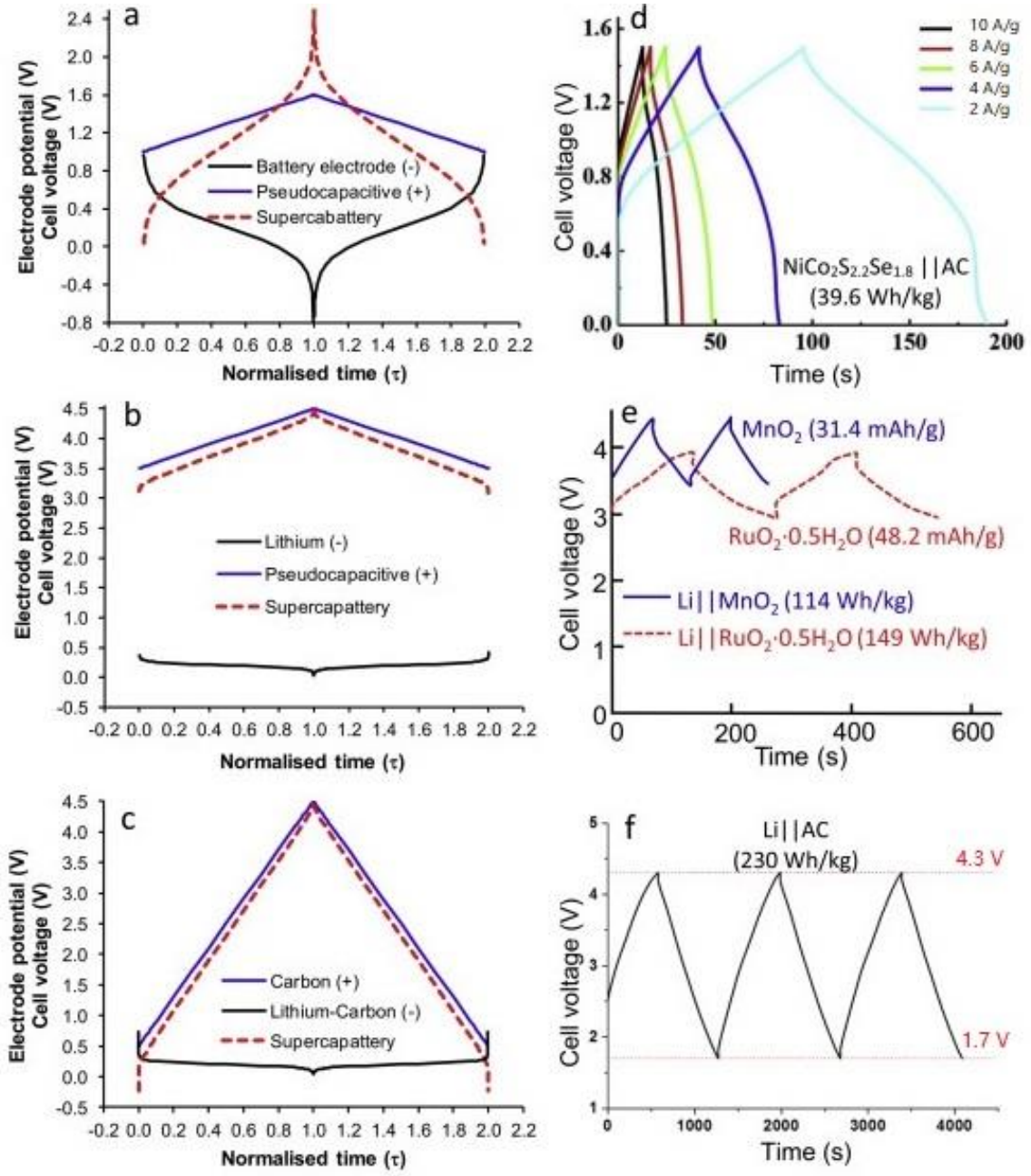

Figure 9. Calculated and experimental GCDs for supercapatteries across three senarios.[87] (a-c) Calculated GCDs depicting potentials of the positrode (blue line) and negatrode (black line), alongside the cell voltage (red dashed lines), normalised over time. These scenarios involve supercapatteries combining a pseudocapacitive positrode of a narrow potential window with a Nernstian negatrode of quasi-reversibility (a), a lithium metal or lithiated carbon negatrode (b), and an activated carbon positrode of a wide potential window with a lithiated carbon negatrode (c). (d-f) Experimentally recorded GCDs depicting the cell voltage against time for three successfully demonstrated supercapatteries with different performances: (d) $NiCo_2S_{2.2}Se_{1.8}$||AC,[88] (e) Li||TMO,[40] and (f) Li||AC.[38] (Reprinted from Ref. 87 with permission from Elsevier).

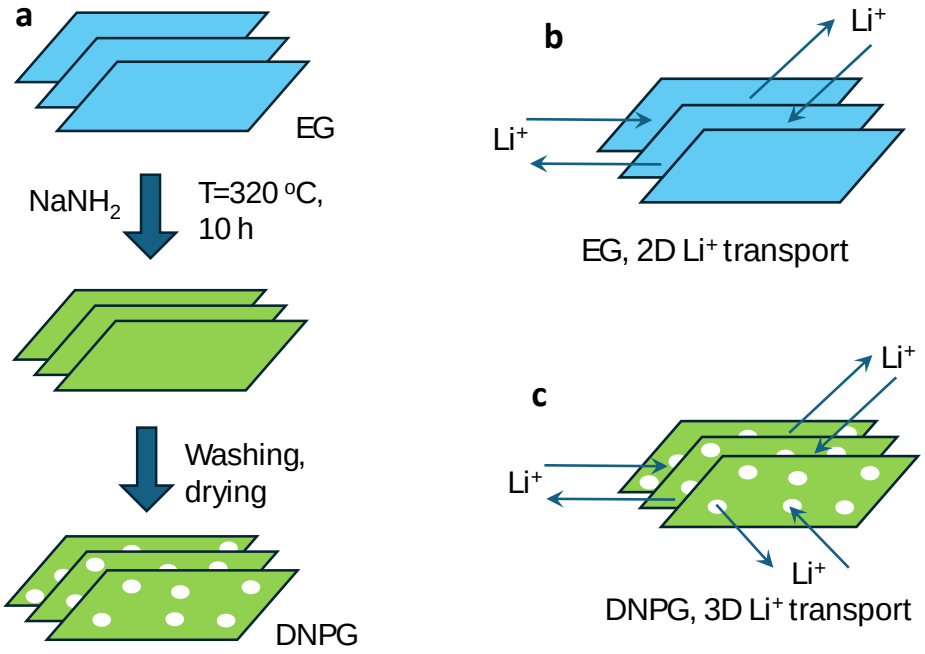

Figure 10. Schematic illustration of (a) the preparation process of DNPG from EG, (b) the 2D and (c) 3D ion transport in graphene stacks with (c) and without (b) in-plane nanopores for shortcuts.[89]

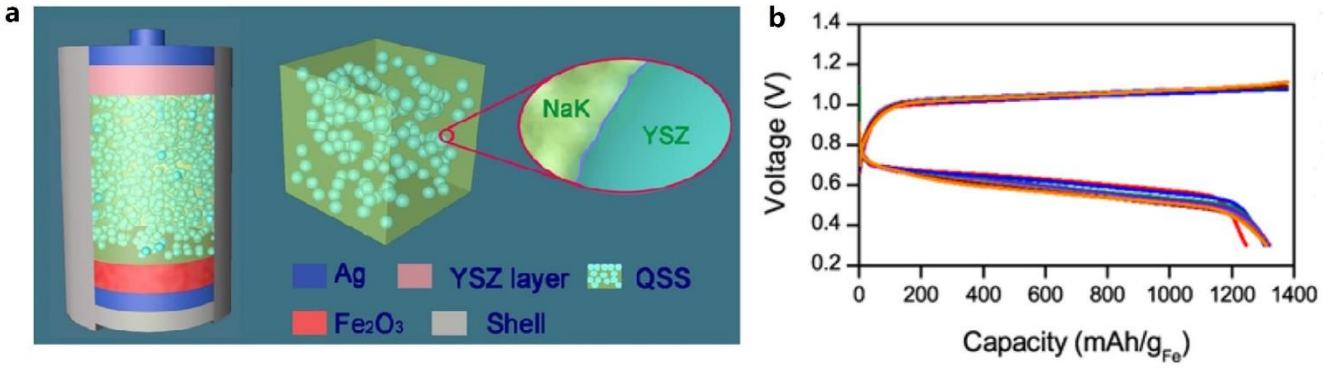

Figure 11. (a) Schematic illustration of QSS molten salt ion-air battery. (b) Charge-discharge curves of QSS molten salt ion-air battery in the 10th (red), 20th (blue), 30th (green), 40th (violet), 50th (gray), 60th (brown), 70th (orange) cycles, respectively.[97] (Redrawn and reprinted from Ref. 97 with permission from Elsevier).

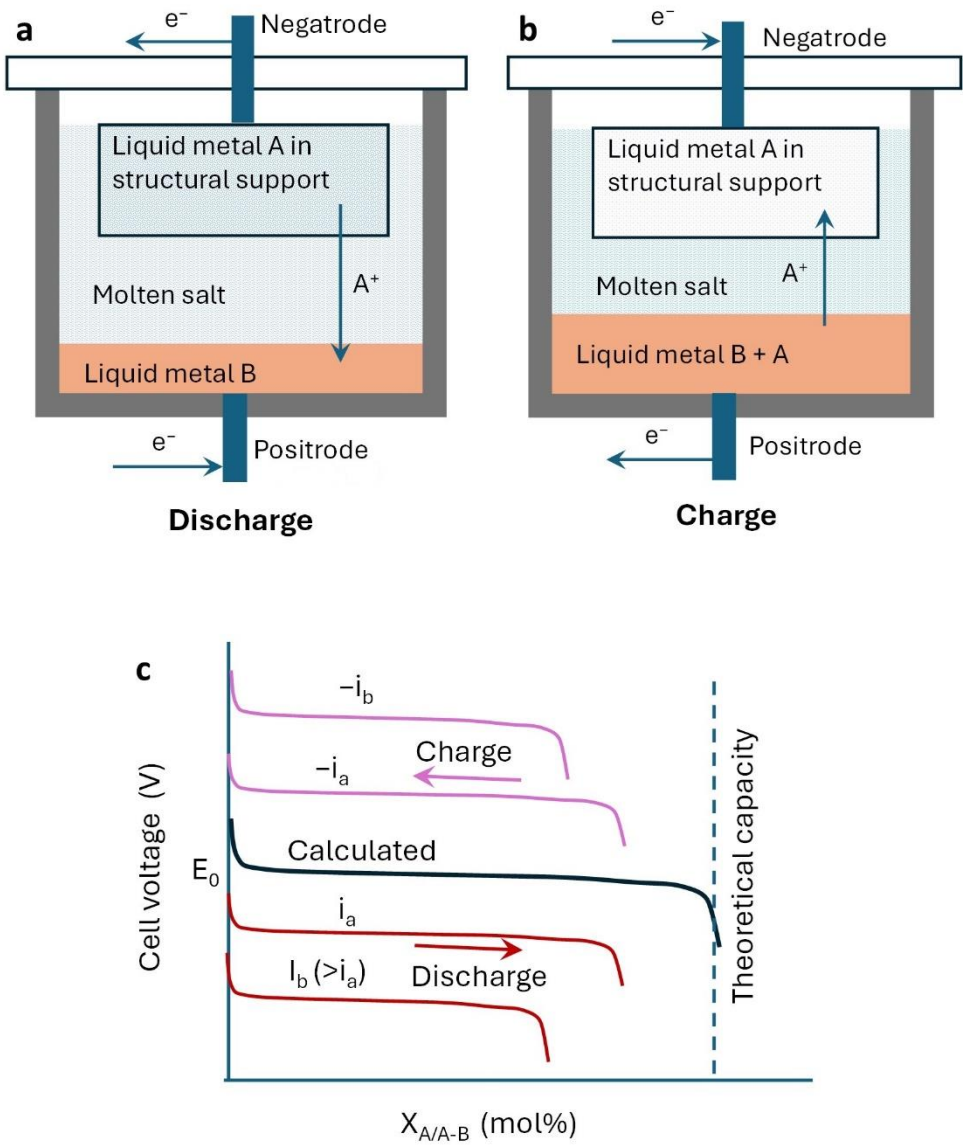

Figure 12. Cell schematics of an all liquid metal battery (e.g. Li | molten LiF–LiCl–LiI | Sb-Pb) during (a) discharge and (b) charge. (c) Calculated and representative practical charge-discharge profiles at different currents, showing the effect of polarisations.[98]

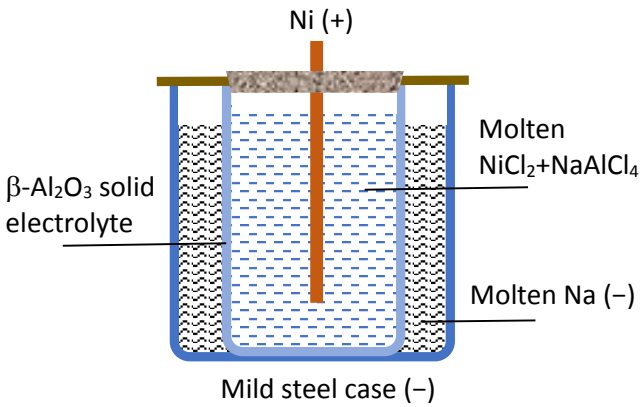

Figure 13. Schematic illustration of a "Na | $NiCl_2$-$NaAlCl_4$ | β-Al_2O_3 | Ni" battery which is widely known as the ZEBRA battery. U: calculated cell voltage of the indicated cell reaction at 300°C.

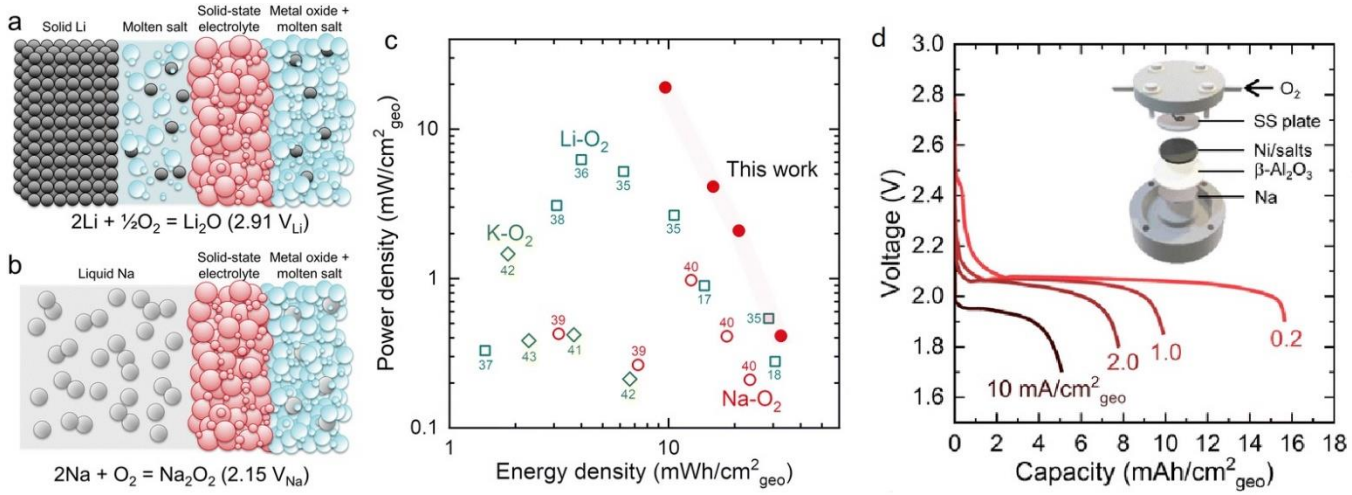

Figure 14. Schematic representation of (a) a molten-salt Li-O_2 battery (b) a molten-salt Na-O_2 battery featuring a liquid Na metal negative electrode, solid-state electrolyte, and metal oxide-based oxygen positive electrode using eutectic salts (e.g., $NaNO_3$ (26.4 wt%)/KNO_3 (27.3 wt%)/$CsNO_3$ (46.3 wt%). (c) A comparison of energy and power densities based on the positive electrode area in a Ragone plot for alkali metal-oxygen batteries. (d) Discharge profiles of molten-salt Na-O_2 batteries at various current densities (0.2, 1.0, 2.0, 10.0 mA cm^{-2}_{geo}).[32] (Redrawn and reprinted from Ref. 32 according to the Open Access License CC By, the Royal Society of Chemistry).

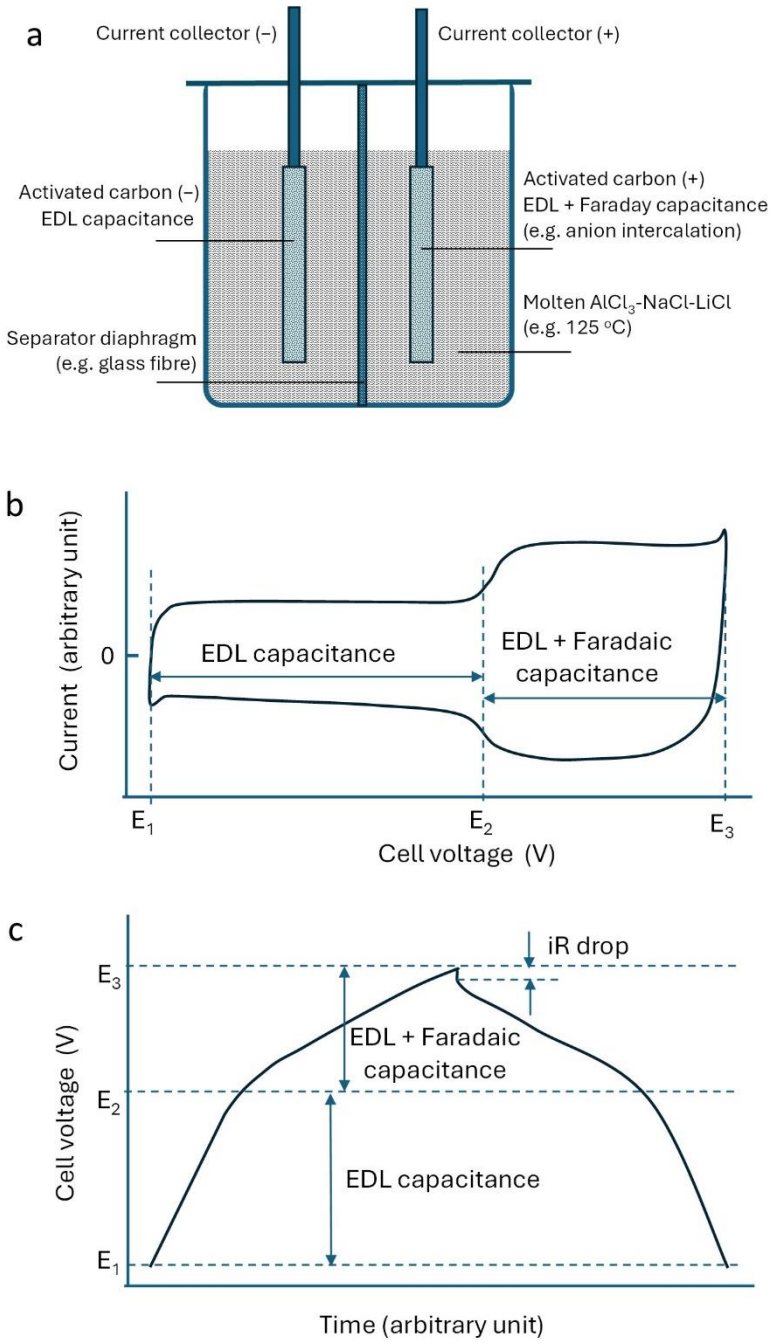

Figure 15. (a) Schematic diagram of a symmetrical activated carbon supercapacitor with a molten mixture of $AlCl_3$, NaCl and LiCl as the electrolyte and anion intercalation in the positrode. Typical (b) CV and (c) GCD of the symmetrical cell showing two stages of the dis-/charging process due to EDL storage and the combined EDL and Faraday (anion intercalation) storage in the positrode at high voltages.[34]

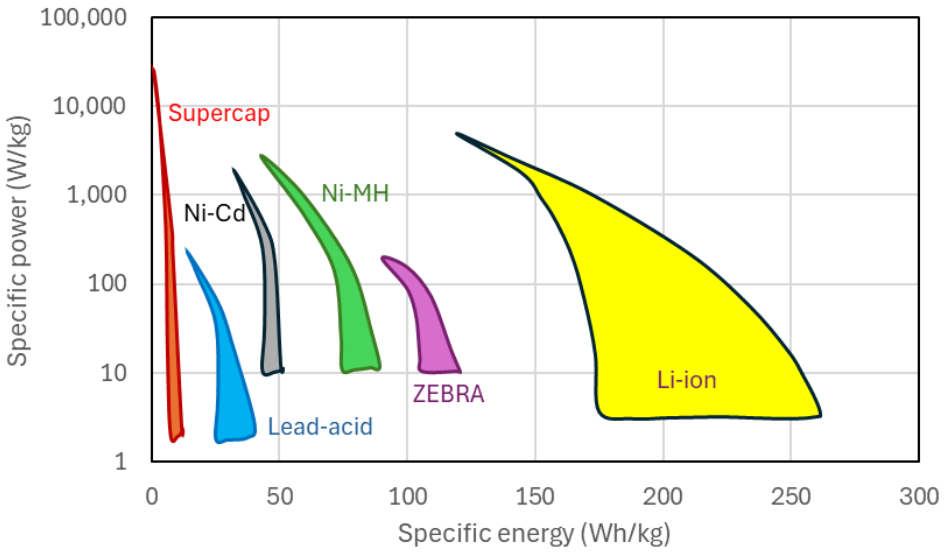

Figure 16. Schematic representations of the Ragone (power vs. energy) profiles of conventional commercial rechargeable batteries in comparison with that of the EDL supercpacitors.[104]

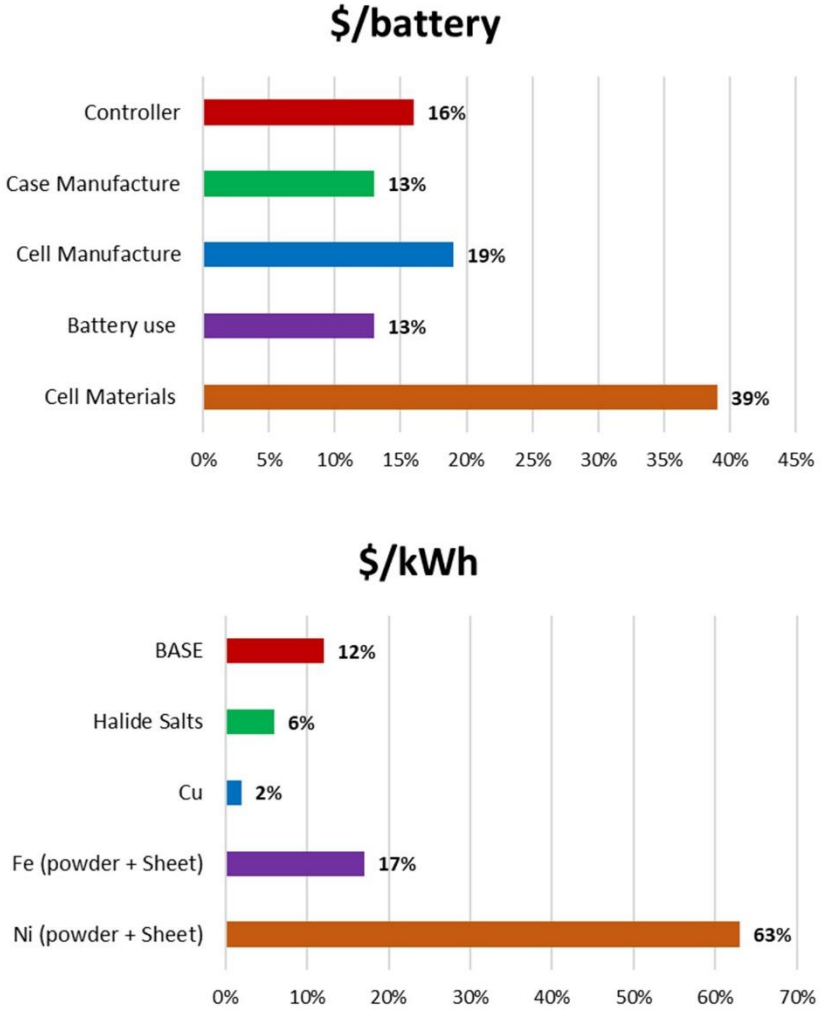

Figure 17. ZEBRA (Na-$NiCl_2$) battery cost breakdown per battery unit (top) and per energy unit (bottom).[106]

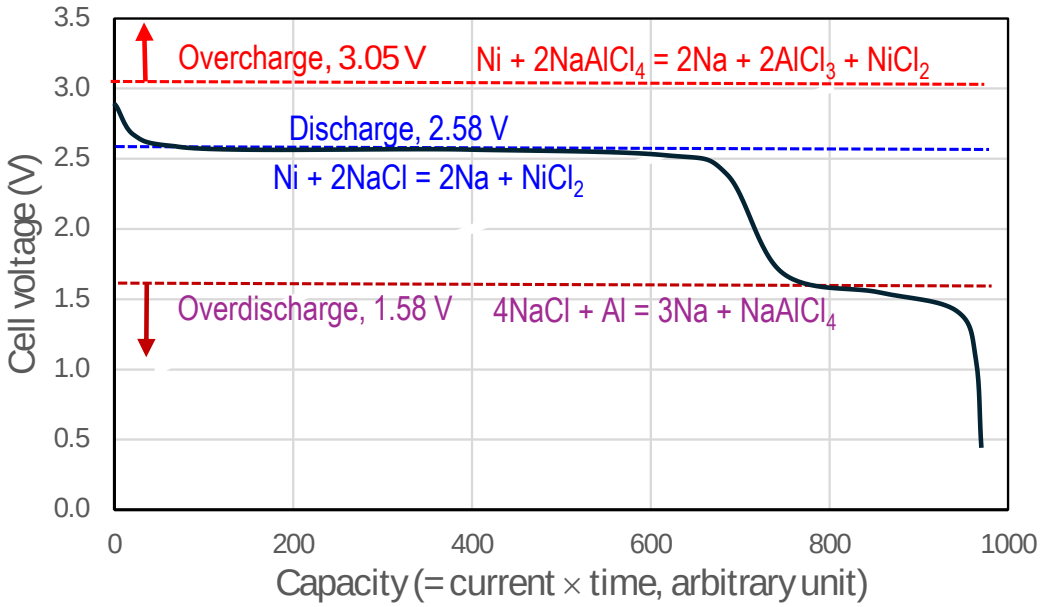

Figure 18. A schematic galvanostatic discharge curve of the ZEBRA (Na-$NiCl_2$) battery at elevated temperatures (e.g. 300 °C), showing the working discharge reaction with those of overcharge and overdischarge reactions.[108,109]

Table 1. Five supercapattery design scenarios corresponding to Fig. 9 (a)-(c). The detailed calculations for specific energy can be found in a prior review article.[36]

Dominant mechanism	Positrode	Negatrode	GCD[a]	Cell voltage, U (V)		W_{sp}[b] (W h kg^{-1})	Reference
				U_{max}	U_{min}		
Battery	Pseudocapacitive type	Typical battery	Fig. 9 (a)	2.5	≥ 0	N/A	[36] (calculated result)
	$NiCo_2S_{2.2}Se_{1.8}$	Activated carbon	Fig. 9 (d)	1.6	0	39.6	[88] (experimental result)
Capacitor	Pseudocapacitive type	Li metal	Fig. 9 (b)	4.5	3.5	555.6	[36] (calculated result)
	Pseudocapacitive type	lithiated carbon (LiC_x, x ≥ 6)	Fig. 9 (b)	4.5	3.5	404.6	[36] (calculated result)
	MnO_2	Li metal	Fig. 9 (e)	4.3	3.3	114	[40] (experimental result)
	$RuO_2 \cdot 0.5H_2O$	Li metal	Fig. 9 (e)	3.8	2.8	149	[40] (experimental result)
	Activated carbon	lithiated carbon (LiC_x, x ≥ 6)	Fig. 9 (c)	4.5	0.5	347.2	[36] (calculated result)

	Activated carbon	Li metal	Fig. 9 (c)	4.5	0.5	555.6	[36] (calculated result)
	Activated carbon	Li metal	Fig. 9 (f)	4.3	1.7	232	[38] (experimental result)

[a]GCD: galvanostatic charge-discharge curve.

[b]W_{sp}: Specific energy.